UNIVERSITÉ DU QUÉBEC À MONTRÉAL

MAGNETIC CARBON-ENCAPSULATED IRON CARBIDE NANOPARTICLES: SYNTHESIS, FUNCTIONALIZATION, AND APPLICATION

THESIS

PRESENTED

AS PARTIAL REQUIREMENT

FOR THE DEGREE MASTER IN CHEMISTRY

BY
MOHAMMED ALAHMADI

FEBRUARY 2016

UNIVERSITÉ DU QUÉBEC À MONTRÉAL

ENCAPSULATION DE NANOPARTICULES À BASE DE CARBURE DE FER MAGNÉTIQUE: SYNTHÈSE, FONCTIONNALISATION ET APPLICATION

MÉMOIRE
PRÉSENTÉ
COMME EXIGENCE PARTIELLE
DE LA MAÎTRISE EN CHIMIE

PAR
MOHAMMED ALAHMADI

FÉVRIER 2016

ACKNOWLEDGEMENT

I would like to express deep gratitude to my supervisor, Prof.Mohamed Siaj, for providing me the chance of taking part in Master. I thank him for all his assistance, guidance and support me through this project, without hem I would not be able to complete my thesis.

Also, the thank goes to the members of the Siaj group, Shimaa, Reda, Jeanne, Fillip and Ons for their excellent assistance and spiritual supports for me during my study. In particular I would like to thank Gaston, for his advices and his friendly assistance with various problems all the time, especially for his help with preparing and build up electrochemical immunosensor assay, and his help outside the lab.

I would like to acknowledge friends and family who supported me during my time here. I would like to thank my close friend, Mohammed Awaji, who as a good friend was always willing to help and gives his supports. I would also like to thank my beloved parents and siblings. They were always supporting me and encouraging me with their best wishes. I must express my gratitude to Afaf, my wife, for standing beside me through my studying.

Finally, I acknowledge Taiba University for financial support. I would like to thank administrative staff members of Saudi Arabian Cultural Bureau especially, Dr.Ali Mohammed Al-bashri and Nancy Gad for their generous support during my study.

DEDICATION

I would dedicate this thesis to
my parents, Naji Alahmadi
and Mariam

TABLE OF CONTENTS

LIST OF FIGURES

LIST OF TABLES

LIST OF ABBREVIATIONS

ACN	Acetonitrile
ADP	Arc Discharge Plasma
AP	P-aminophenyl
Ar	Aryl ring
BE	Binding energy
$C_{16}H_{36}F_6NP$	Tetrabutmmonium hexafluoro-phosphate
C_2H_6O	Ethanol
C_3H_7NO	Dimethyl forma amide
$C_5H_8O_2$	Glutaraldehyde
$C_6H_4N_3O_2 \cdot BF_4$	P-nitrobenzenediazonium tetrafluoroborate
CE	Counter electrode
CH_3CN	Acetonitrile
CVD	Chemical vapor deposition
DMF	N, N-dimethyl formamide
E	Potential
EDS	Energy dispersive x-ray spectroscopy
FT-IR	Fourier transforms infrared spectroscopy
FWHM	Full width at half maximum

GA	Glutaraldehyde
HR-TEM	High resolution Transmission electron microscopy
I	Current
K_2HPO_4	Dipotassium phosphate
$K_3Fe(CN)_6$	Potassium ferricyanide
KH_2PO_4	Monopotassium phosphate
MKP	Monopotassium phosphate
MNPs	Metal nanoparticles
Ms	Saturation magnetization
MWCNT	Multi-Walled Carbon Nanotubes
$NaHCO_3$	Sodium bicarbonate
NaOH	Sodium Hydroxide
NBDT	Nitrobenzenediazonium
NPs	Nanoparticles
PB	Phosphate buffer
PBS	Phosphate buffered saline
RT	Room temperature
S	Sulfur
SAED	Selected Area Electron Diffraction
SEM	Scanning electron microscopy
SPCE	Screen-printed carbon electrodes
SWV	Square wave voltammetry

TEM	Transmission electron microscopy
XPS	X-ray photoelectron spectroscopy
XRD	X-ray diffraction
β –LG	β-lactoglobulin antibody

LIST OF UNITS

A	Ampere
Cm	Centimeter
eV	Electronvolt
g	Gram
h	Hour
I	Electric current
K	Kelvin
Mg	Milligrams
mg/l	Milligrams per liter
min	Minutes
ml	Milliliter
mol	Mole
ng/ml	Nanogram per milliliter
nm	Nanometer
°C	Temperature
Oe	Oersted
Pg	Picogram

S	Second
T	Time
V	Voltage
μ	Micro
μg	Micrograms
μg/g	Microgram per gram
μg/l	Microgram per liter
μl	Microliter
μm	Micrometer

RÉSUMÉ

Les principaux objectifs de ce travail de recherche ont été la production, la fonctionnalisation et la caractérisation des particules ayant des nanostructures coeur-coquille (*Core-Shell*) FeC@Graphene/Graphene. La synthèse a été réalisée par le dépôt en phase vapeur par procédé chimique (CVD) à 950 ^{0}C pendant 60 minutes. Les nanoparticules (NPs) obtenues affichent un comportement super-magnétique. Les nanoparticules FeC@Graphene ont été utilisées pour la fabrication d'un immunocapteur pour la détection de la β-lactoglobuline. Après la fonctionnalisation chimique des NPs, elles ont été déposées sur des électrodes de carbones sérigraphiées (SPCE). La caractérisation des FeC@Graphene/Graphene a été réalisée par des techniques d'analyse comme la microscopie à transmission d'électrons à haute résolution (HR-MET) et par la diffraction d'électrons dans une zone sélectionnée. La HR-MET a montré que des nanoparticules de fer ayant une nanostructure coeur-coquille avec des tailles variant entre 20 et 80 nm. Les nanoparticules FeC@Graphene ont été fonctionnalisées avec des groupes d'amines via une réaction spontanée avec le P-nitro benzenediazonium tetrafluoroborate (P-NBDT) et suivi par une réduction des groupes nitro. Les groupes amine et après activation ont été liées à la glutaraldéhyde. Ces derniers ont été utilisés pour l'immobilisation covalente d'anticorps monoclonaux, le anti-ß-lactoglobuline (mAb).Chaque étape du processus de la fonctionnalisation des NPs a été étudiée par la spectroscopie infrarouge, les techniques de microscopie électronique et la spectroscopie à rayons X. Une approche électrochimique par la technique de voltammétrie d'onde carré (SWV) a été utilisée pour lier la β-lactoglobuline et l'immunocapteur. L'interaction entre la β-lactoglobuline et les NPs fonctionnalisées sur les électrodes de carbone sérigraphiées a entraîné une baisse apparente (considérable) du signal de réduction de la voltammetrie d'onde carrée du couple redox $[Fe(CN)6]^{4-/3-}$. Dans des conditions optimales, la limite de détection de l'immunocapteur développé montre une haute sensibilité et a une limite de détection à l'ordre de 0,01 pg/mL. L'immunocapteur résultant sous l'effet d'un champ magnétique externe a permis le dépôt facile et le contrôle des NPs durant leurs contacts avec l'électrode de carbone.

MOTS-CLÉS: nanoparticules magnétiques, techniques de fonctionnalisation, immunocapteurs et β-lactoglobuline.

ABSTRACT

In this work, we describe a sensitive label-free immunosensor for the detection of β-lactoglobulin, based on using fictionalized magnetic FeC nanoparticles NPs upon the screen-printed carbon electrodes (SPCE). To achieve the developed immunosensor, additional materials were used such as synthesized and functionalized magnetic FeC nanoparticles (NPs). Superparamagnetic carbon-encapsulated iron carbide nanoparticles, were produced from pure ferrocene by chemical vapor deposition (CVD) performed to pure Fe powder at 950 C for 60 min. High-resolution transmission electron microscopy (HR-TEM) and selected area electron diffraction patterns showed that Iron nanoparticles were formed as inner cores with sizes ranging from approximately 60 to 80 nm. The functionalized magnetic FeC nanoparticles to get amine groups as linkers was carried out by a spontaneous reaction with P-nitro benzenediazonium tetrafluoroborate (*P*-NBDT) followed by the reduction of nitro groups produced by the elemental sulfur reduction chemistry. Next, the amine groups on the magnetic nanoparticles were activated using glutaraldehyde and used for the covalent immobilization of Anti-b-lactoglubulin monoclonal antibodies (mAb). Each step of functionalization NPs was investigation by (FT-IR) infrared spectroscopy, X-ray diffraction, electron microscopy techniques, and X-ray spectroscopic. An novel electrochemical immunosensor was built up by using square wave voltam-metry (SWV) technique for the determination of β-lactoglobulin based on the change of the $[Fe\ (CN)_6]^{3-/4-}$ reduction peak current due to the specific binding of the β-lactoglobulin with the antibody immobilized on magnetic FeC nanoparticles on the screen-printed carbon electrodes (SPCE) . The resulting immunosensor exhibits high-sensitivity with the detection limit of 0.01 pg/mL and has good corresponding correlation coefficients $R^2 = 0.9909$ in the linear ranges of 0.1 to 100 ng/mL of β-lactoglobulin in PBS buffer. In the developed system, the immunosensor preparation steps were reinforced by means of an external magnetic field to easily deposit and controlled placement the nanoparticles on a working carbon electrode.

Keywords: Magnetic nanoparticles, functionalization techniques, Characterization, Immunosensor, and β-lactoglobulin

CHAPTER I

INTRODUCTION

A general introduction of the magnetic nanoparticle properties and applications is presented in this chapter. Also. The formation mechanisms and techniques used for producing this kind of nanoparticles are described. Furthermore, this chapter describes the advantages of this method for synthesis iron nanoparticles encapsulated with graphene sheets by chemical vapor deposition (CVD).

Nanomaterials are defined as having a size regime of less than 100 nanometers (De La Escosura-Muñiz, Parolo, & Merkoi, 2010). In recent years there has been a great progress in nanoparticles development field including the possibility to synthesis different sizes with different chemical nature and structures. From the material point of view, the NPs exhibit chemical and physical characteristics that are often not observed in the bulk material. This significant difference can be explained by different reasons: (i) Nanoparticles are intermediate objects between bulk systems and atoms. Indeed, increasing the number of atoms in a nanoparticle (from a single atom to a bulk body) induces significant physical and chemical changes on it

(quantum-chemical description). (ii) The fraction of surface atoms in a nanoparticle is comparable to that of bulk atoms; consequently, the surface contribution gives rise to new properties and even novel, unusual structural states. (iii) The size of nanoparticles becomes comparable to the characteristic scale of variation in the physical properties of a material (the size effect). (iv) Since the small size of nanoparticles makes collective excitations with wavelengths in excess of the nanoparticle sizes impossible, the thermodynamic properties of the nanoparticles change significantly (the so-called finite size effect)(Komogortsev et al., 2007). Figure 1.1 shows the tendency in publications about nanoparticles. The number of publications has increased exponentially due to their wide applications in different fields such as medicine, chemistry, and physics and so on. Moreover, not only scientific publications have been growing in the last decades but also a huge number issued patents (Domènech et al., 2012). Metal nanoparticles (MNPs) have attracted increasing interest of scientists and technologists during the last decade, due to their unique physical and chemical properties from bulk metals (e.g., lower melting points, higher specific surface areas, specific optical properties, mechanical strengths, and specific magnetizations), properties that might prove attractive in various industrial applications (Horikoshi, S. and Serpone, 2013). The shape and size distribution of the magnetic materials are the key factors that determine their chemical and physical properties (Amara, Grinblat, & Margel, 2012). Nanoparticles with magnetic properties, superparamagnetism, quantum tunneling, (Oropeza, Corea, Gómez-Yáñez, Cruz-Rivera, & Navarro-Clemente, 2012) high coercivity, low Curie temperature,

high magnetic susceptibility of magnetization, has received considerable attention because they have a wide variety of biomedical applications, such as their uses as contrast enhancement agents for magnetic resonance imaging (MRI), bioprobes and cell sorters (Andrade et al., 2009)(Wu, He, & Jiang, 2008)(Akbarzadeh, Samiei, & Davaran, 2012).

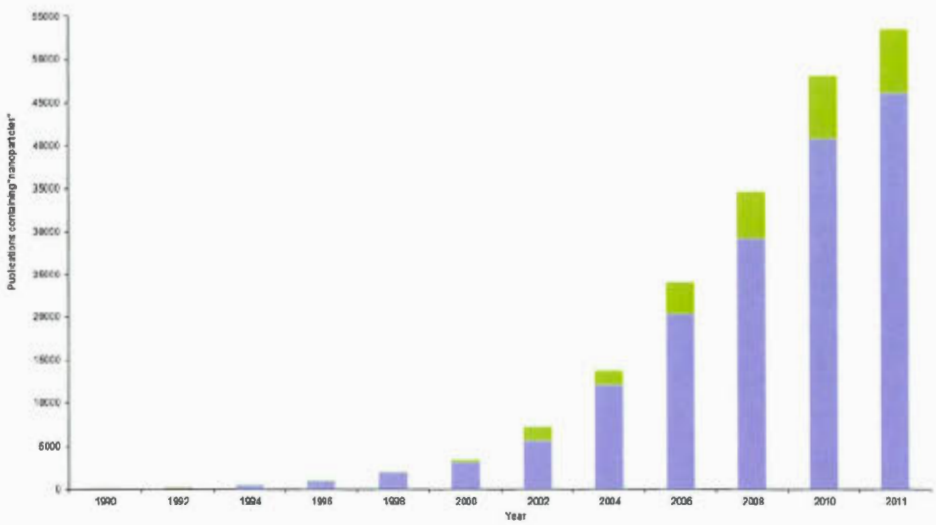

Figure 1. 1 Bibliographic analyses based on the search of "nanoparticles" in Scifinder Scholar. Blue represents scientific publications (e.g. books, articles, reviews) and green represents patents (Domènech et al., 2012).

1.2 Iron-based core–shell nanoparticles

1.2.1 Core-shell nanoparticles

An interesting magnetic nanoparticle system is a core/shell structured nanoparticles in which the magnetic core is coated with a layer of non-a nonmagnetic, antiferromagnetic, or ferro/ferroimagnetic shell. The magnetic a core made from one metal material (e.g. cobalt, iron oxide, etc.)) and shells or coating made from a second material that can provide not only a protection to the core but also a platform for the surface functionalization of the NPs (see Figure 1.2).

The Nanometer-sized magnetic metal carbides iron are receiving great interest due to their enhanced catalytic, electronic, and magnetic properties, which have applications in catalysis, magnetic recording, magnetic fluids, and biomedical applications (Huo, Song, & Chen, 2004) (Zhang, Liang, Liu, Tian, & Shao, 2013). However; pure iron nanoparticles are chemically unstable in the air and easily oxidized, which limits their utility. To protect the particles from oxidation, one way is to coat the particles with another inert layer, namely, making a core–shell structure. Graphene shells of magnetic NPs is capable of maintaining favorable magnetic properties of metal iron and protect the core containing iron nanoparticles against oxidation, and prevent their spontaneous agglomeration and modify the properties (Inagaki, 2012)(Fedoseeva et al., 2012). Also, Graphene covering has many advantages over other coatings, such as much higher chemical and thermal stability, and easy for chemical functionalization.

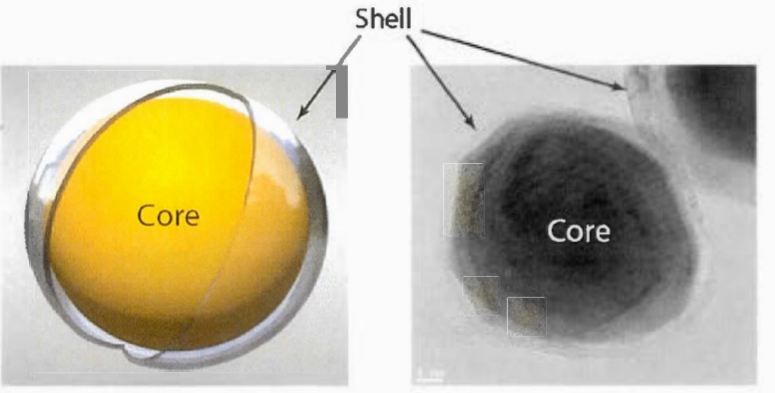

Figure 1. 2 Schematic display of the core/shell nanoparticle architecture indicating core metal and graphene shell. TEM image of our sample shows core/shell FeC@Graphene NPs

1.2.2 Graphene-shell

Graphene is a single layer of carbon atoms arranged in a hexagonal lattice and one of the few 2D structures that are stable at ambient media (Quintana, Spyrou, & Grzelczak, 2010). The graphene is a starting material for different important allotropes; it can be stacked to form 3D graphite, rolled to form 1D nanotubes, and wrapped to form 0D fullerenes (see Figure.1.3) (Katsnelson, 2007).

- 0D Fullerenes.

The fullerenes are molecules where carbon atoms are arranged spherically, and hence, from the physical point of view, are zero- dimensional objects with discrete energy states. The fullerenes can be obtained from graphene with the introduction of pentagons (that create positive curvature defects), and hence, fullerenes can be thought as wrapped-up graphene (V. Singh et al., 2011).

- 1D Carbon nanotubes.

Carbon nanotubes are obtained by rolling graphene along a given direction and reconnecting the carbon bonds. Hence carbon nanotubes have only hexagons and can be thought of as one-dimensional 1D objects (V. Singh et al., 2011). The properties of nanotubes depend on atomic arrangement (on how the sheets of graphite are 'rolled'), the diameter and length of the tubes, and morphology, or nano structure({In-Yup Jeon, Dong Wook Chang, Nanjundan Ashok Kumar, 2011).

- 3D Graphite.

Graphite, Graphite consists of individual graphene layers, each composed of interlinked hexagonal carbon rings tightly bonded to each other, stacked loosely into a three-dimensional material (Crespi, 2004).

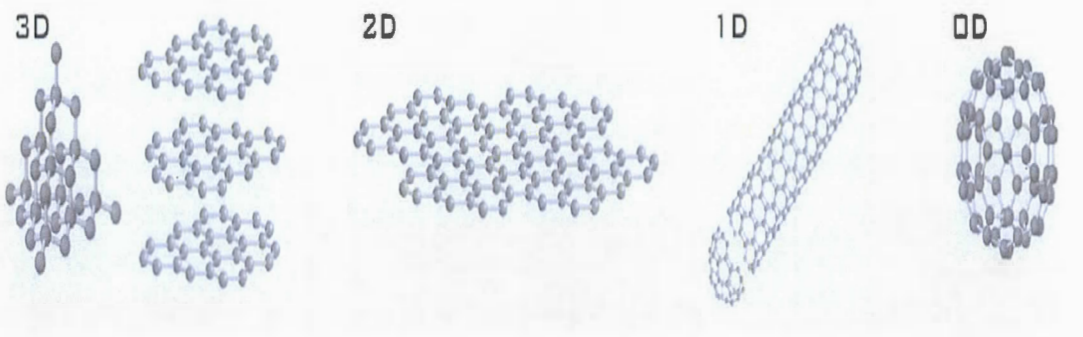

Figure 1. 3 Crystal structures of the different allotropes of carbon (Left to right) Three-dimensional diamond and graphite (3D); two-dimensional graphene (2D); one-dimensional nanotubes (1D); and zero-dimensional buckyballs (0D)(Katsnelson, 2007).

1.3 Synthesis Mechanism: nanoparticle formation and Growth

1.3.1 Nucleation

The nucleation can be defined as the formation of a new phase in a distinct region, separated from the surroundings by a definite boundary. The nucleation is of two types, namely, homogeneous nucleation and heterogeneous nucleation. Homogeneous nucleation does not involve foreign atoms, particles or surfaces. Heterogeneous nucleation is achieved through the influence of foreign particles and/or surfaces (Mwamba, 2005). The process of homogeneous nuclei formation can be considered thermodynamically by looking at the total free energy of a nanoparticle defined as the sum of the surface-free energy and the bulk-free energy. For a spherical particle of radius r, the surface energy γ and the free energy of the bulk crystal ΔG_V, giving a total free energy ΔG, eq 1.

The crystal-free energy itself, ΔG_V is dependent upon the temperature T, Boltzmann's constant k_B, the supersaturation of the solution S, and its molar volume, v. ΔG_V is defined in **eq 2.**

$$\Delta G = 4\pi r^2 \gamma + 4/3\pi r^3 \Delta G_V \qquad (1)$$

$$\Delta G_V = -k_B T \ln (S)/v \qquad (2)$$

Due to the surface-free energy always being positive and the crystal-free energy always being negative, it is possible to find a maximum free energy which a nucleus will pass through to form a stable nucleus by differentiating ΔG with respect to r and setting it to zero, $d\Delta G/dr = 0$, which gives a critical free energy, **eq 3**. By the way, the critical radius is defined in eq 4:

$$\Delta G_{Crit} = 4/3\ \pi\gamma r_{crit} = \Delta G_{crit} \qquad (3)$$

$$r_{Crit} = -2\pi/\Delta G_V = -2\pi v/k_B T \ln S \qquad (4)$$

This critical radius corresponds to the minimum size at which a particle can survive in solution without being redissolved. The same is true for the particle's free energy, where a critical free energy is required to obtain stable particles within the solution, Figure1.4 (Thanh, Maclean, & Mahiddine, 2014).

From this Figure, one can easily see that the newly formed nucleus is stable only when its radius exceeds a critical size, r_c. A nucleus smaller than r_c will dissolve into the solution to reduce the overall free energy, whereas a nucleus larger than r_c is stable and continues to grow bigger.

The above discussion was based on a supersaturated solution; however, all the concepts can be generalized for a supersaturated vapor and a supercooled vapor or liquid. In the synthesis and preparation of nanoparticles by nucleation from supersaturation solution or vapor, this critical size represents the limit how small nanoparticles can be synthesized. To reduce the critical size and free energy, one needs to increase the change of Gibbs free energy, ΔG_V, and reduce the surface energy of the new phase, γ (Guozhong Cao, 2010).

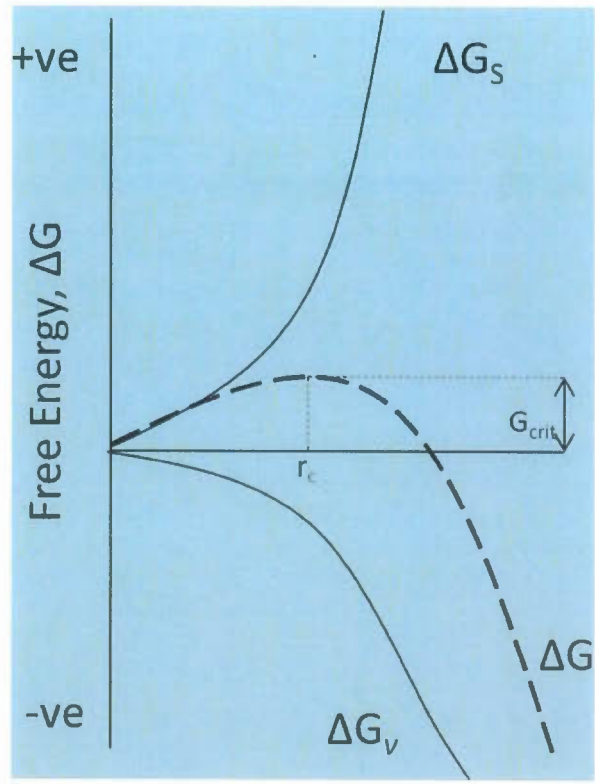

Figure 1. 4 Free energy diagram for nucleation explaining the existence of a "critical nucleus" (Thanh et al., 2014).

1.3.2 Subsequent growth of Nuclei

The size distribution of nanoparticles is dependent on the subsequent growth process of the nuclei. The growth process of the nuclei involves multi-steps and the major steps are (i) generation of growth species, (ii) diffusion of the growth species from bulk to the growth surface, (iii) adsorption of the growth species onto the growth surface, and (iv) surface growth through irreversible incorporation of growth species onto the solid surface. These steps can be further grouped into two processes.

Supplying the growth species to the growth surface is termed as diffusion, which includes the generation, diffusion, and adsorption of growth species onto the growth surface, whereas incorporation of growth species adsorbed on the growth surface into solid structure is denoted as growth. Diffusion-limited growth would result in a different size distribution of nanoparticles as compared with that by growth-limited process (Guozhong Cao, 2010).

1.4 Size Nanoparticles

Atoms at the surface of small particles have various physical properties (mechanical strength, ductility, thermal stability, sintering ability, and diffusivity) quite different from those of the same atoms at the surface of a large particle. Even a corner or edge atom is chemically different from an atom embedded in the middle of a surface face or an atom sitting on top of the same crystal face (Roduner, n.d.) (Ghosh, 2011). There are major factors those are responsible for these differences:

1.4.1 Fraction of atoms at the surface

The surface effect reflects that the stabilization of an atom in a solid or liquid environment scales with the number of neighbors to which it can make bonds. The temperature of melting or of any other phase transition relates to this stabilization and therefore to the average number of neighbors. This leads to a smooth scaling law of transition temperature with a particle radius or thickness of a layer or wire. The total number of atoms N in this sphere scales linearly with volume. The fraction of atoms

at the surface is called dispersion F, and it scales with a surface area divided by volume. The surface area of a sphere, $A= 4\pi r^2$, divided by its volume, $V=4\pi r^3/3$, is $3/r$, or in terms of diameter d, $6/d$. Neglecting edge effects, the $F= A/V$ for large, thin plates of thickness d equals $1/d$, and also for long, cylindrical wires $F=1/d$.

Thus, for anybody where a single narrow thickness d is defined the dispersion scales smoothly with $1/d$. This is the basis for the explanation of many observed properties, which scale smoothly as $1/d$ or $1/r$, indicating that it is a surface effect. The size dependence of dispersion is illustrated in Figure 1.5 for cubes of n atoms along an edge and a total of $N=n^3$ atoms, where the number of atoms at the surface is 6n corrected for double counts at the 12 edges and for reinstalling the 8 corners. For large N the edge and corner corrections become negligible, leading to the $N^{-1/3}$ scaling:

$$F= 6n^3 -12n + 8/n^3 = 6/N^{1/3} (1 - 2/N^{1/3} + 8/6N^{2/3}) \approx 6/N^{1/3}$$

All properties, which depend on the dispersion of a particle, lead to a straight line when plotted against r^{-1}, d^{-1} or $N^{-1/3}$. Atoms at the surface have fewer direct neighbours than atoms in the bulk. Therefore, particles with a large fraction of atoms at the surface have a low means coordination number (which is the number of nearest neighbours). In fact, the dispersion and the mean coordination number <NN> obey the same scaling law and are equivalent measures of surface effects (Roduner, 2006) (Roduner, n.d.).

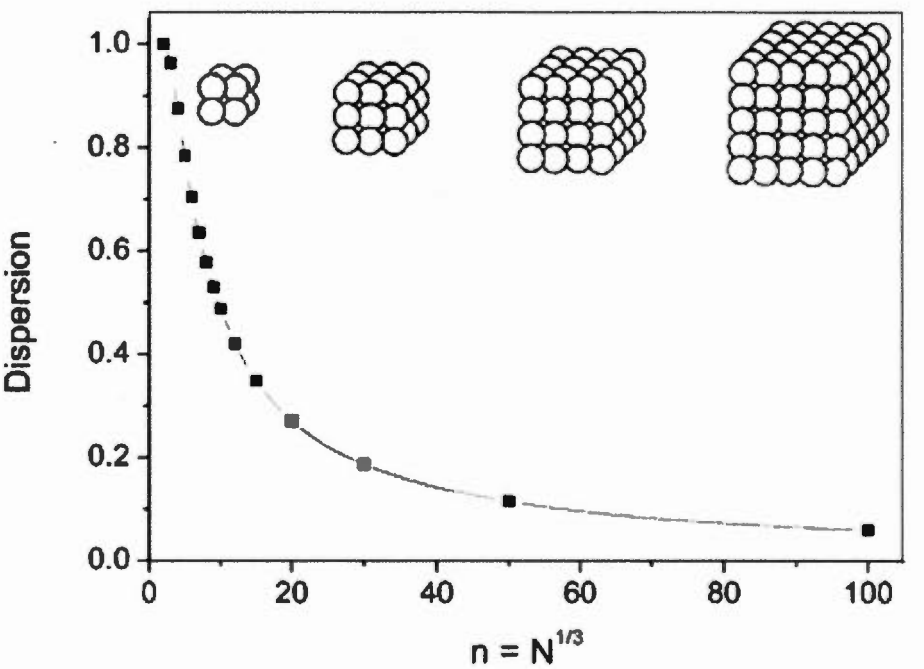

Figure 1. 5 Evolution of the dispersion F as a function of n for cubic clusters up to n = 100 ($N = 10^6$). The structure of the first four clusters is displayed (Roduner, 2006)

1.4.2 Quantum confinement effect

The quantum confinement effect is a consequence of quantum mechanics and of the particle wave duality. Electrons behave at the same time as particles and as waves. As waves they explore the entire space in which they are free to move (Roduner, n.d.). The origin of quantum confinement in so-called zero-dimensional nanocrystallite, such as quantum dots (QDs), is understood to arise from the spatial confinement of electrons within the crystallite boundary. Quantum confinement lead to increases the spacing between energy levels as the nanocrystallite size is decreased (Andersen, Fong, & Pickett, 2002).

In the nanometer regime various physical properties, such as, mechanical strength, ductility, thermal stability, sintering ability, diffusivity and the chemical reactivity of the particles have also been found to be dependent on particle size without a change in the chemical composition of the particles. A root cause for this behaviour is that in the bulk material (several times bigger than 10 nm), charge carriers can have a range of energies. These energies are so close together that they can be described as continuous (see Figure 1.6).

However; for small particles with dimensions in the nanometer regime; the electronic states are not continuous as in the bulk, but are discrete, due to the confinement of the electron wave function in finite physical dimensions of the particle (Chukwuocha, 2012) (Thomas & Kulkarni, 2003). From Figure 1.6 we can see that ΔE_{nano} is greater than ΔE_{bulk} this is due to the reduction in dimensions of the QD, which increases the confinement energy in the dot nanoparticle. The average electronic energy level spacing of successive quantum levels, δ, known as the so-called Kubo gap, is given by, $\delta = 4E_f/3n$, where E_f is the Fermi energy of the bulk material and n the total number of valence electrons in the nanocrystal (Thomas & Kulkarni, 2003).The Kubo gap it is measured in units of millielectron volts (meV) Since, the number of valence electrons in the nanoparticles is measured as a function of nuclearity, the energy level spacing varies inversely with the nuclearity of the particles as shown in Table 1 (Ghosh, 2011).

Table 1: Characteristic parameters showing the relationship between the diameter, nuclearity and Kubo gap in metal nanoparticles (Ghosh, 2011)

System	Diameter (nm)	Nuclearity	Kubo Gap (in K)
A	$>> 10^3$	$>> 10^{10}$	10^{-6}
B	10^3 - 10	10^{10} - 10^4	10^{-6} - 1
C	10 - 1	10^4 – 10	1 - 10^3
D	<1	> 10	> 10^3

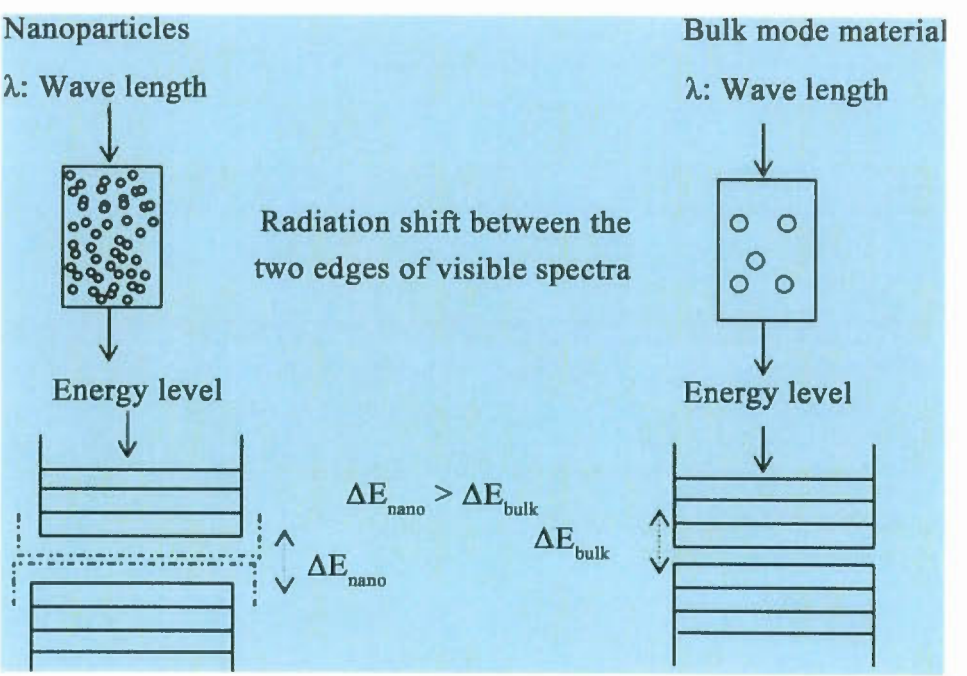

Figure 1. 6 Quantum confinement is responsible for the increase of energy difference between energy states and band gap.(Chukwuocha, 2012)

1.4.3 Superparamagnetic

The size of the magnetic nanoparticles affected by the nanoparticle's regime and hence magnetic behavior as shown in Figure 1.7. As the size of the magnetic nanoparticles (MNP) decreases, the magnetic anisotropy energy per nanoparticle decreases. Magnetic anisotropy energy is the energy that keeps the magnetic moment in a particular orientation.

At a characteristic size for each type of MNP, Superparamagnetic occurs in ferromagnetic materials (Fe, Ni, Co) when the anisotropy energy becomes equal to the thermal energy, which allows the random flipping of the magnetic moment flipping occurs at sizes below $\mathbf{r^o}$. At a characteristic size for each type of MNP, Superparamagnetic occurs in ferromagnetic materials (Fe, Ni, Co) when the anisotropy energy becomes equal to the thermal energy, which allows the random flipping of the magnetic moment and the flipping occurs at sizes below r_o.

The magnitude of saturation magnetization ***Ms*** also strongly depends on the size of the nanoparticle and is described by Equation (3). MNPs possess a disordered spin layer at their surfaces, and when the size of the nanoparticle is small (<5 nm), the ratio of disordered layer to the radius of the MNP is significant (Kolhatkar, Jamison, Litvinov, Willson, & Lee, 2013). Surface spin disorder thus leads to reduced Ms for smaller nanoparticles as defined here:

$$\mathbf{Ms = Ms_b[(r-d)/r]^3} \qquad \mathbf{(3)}$$

Where r is the radius, d is the thickness of the MNP surface exhibiting disordered spins, and Ms_b is the bulk Ms.

Magnetic moment not only depends on the number of atoms, but also depend on the cluster structure. Figure 1.8 shows the magnetic moment of several clusters belonging to Fe clusters. The magnetic moment is found to decay as a function of cluster size; clusters with faceted surfaces are predicted to have magnetic moments lower than clusters with non-faceted surfaces. As a consequence, clusters with many atoms protruding from the surface, are expected to have strong magnetic properties at fixed temperatures. In addition, large clusters with icosahedral structure are expected to have magnetic moments lower than clusters with BCC structure (Tiago, Zhou, Alemany, Saad, & Chelikowsky, 2006).Furthermore, the bulk of ferromagnetic material consists of a number of small regions of magnetons, which are called domains as shown in Figure 1.9. The boundaries between domains are called domain walls.

Thus, a magnetic domain in a ferromagnetic material refers to the volume of the material in which all magnetons are aligned in the same direction by the exchange forces. This concept of domains distinguishes ferromagnetism from paramagnetism. The ferromagnetic material in a demagnetized state does not show any magnetization as the total magnetization is canceled because of the random orientation of the magnetizations in magnetic domains. However, on the application of an external

magnetic field, the magnetic domain walls are washed away and magnetic moments become aligned to the direction of the magnetic field and saturate the magnetization Figure 1.9. This magnetization is called saturation magnetization (Ms) Figure 1.10. On removal of the applied magnetic field, instead of retracing its original path, ferromagnets retain some memory of the applied field called as remanence (Point A in the curve, Figure 1.10). To reduce the magnetization of that material to zero, a coercive force (Pont B in the Curve, Figure 1.10) must be applied to a ferromagnetic material so as to close the loop. Thus coercivity measures the resistance of a ferromagnetic material to become demagnetized. This behavior of the ferromagnetic material is known as the hysteresis and the path, which it follows, is known as the hysteresis loop in Figure1.10. Due to its varied dependence on the magnetic field, the ferromagnetic materials can be categorized into soft and hard magnetic materials Figure 1.10 (Mody, Singh, & Wesley, 2013).

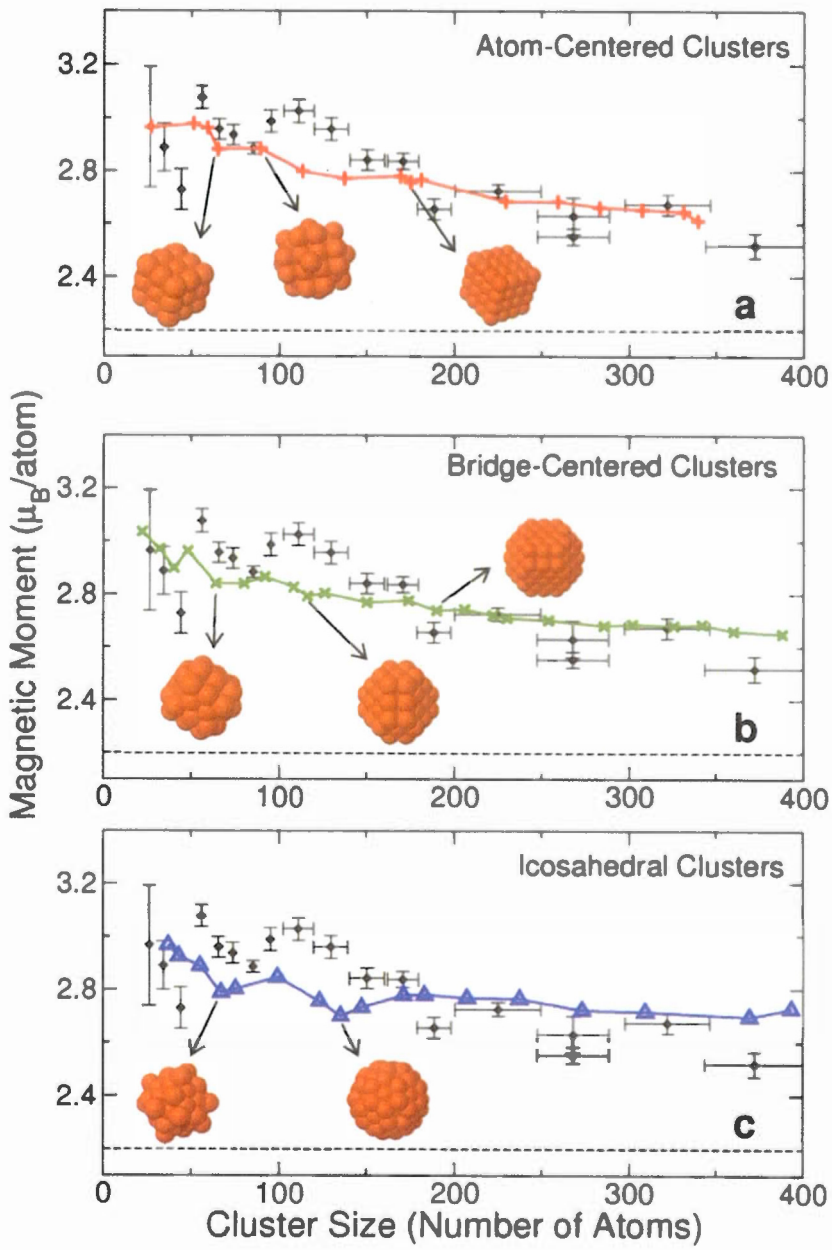

Figure 1. 7 Calculated magnetic moments for clusters in the atom-centered ("plus" signs, a), bridge-centered (crosses, b), and icosahedral (triangles, c) families. The dashed lines indicate the value of the magnetic moment per atom in bulk iron (Tiago et al., 2006).

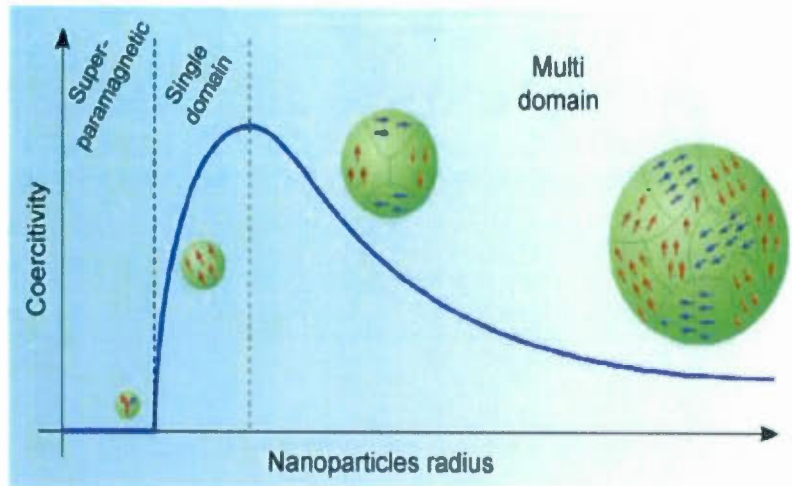

Figure 1. 8 Schematic illustrations of the coercivity-size relations of small particles. Copyrighted from reference (Mody et al., 2013).

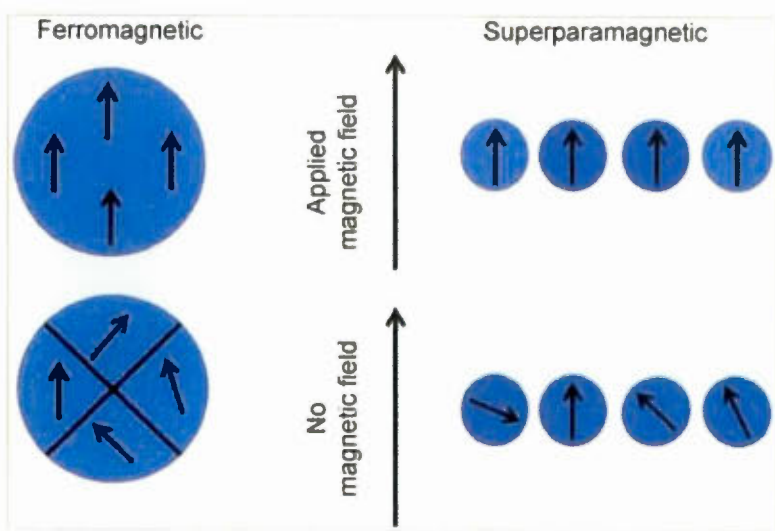

Figure 1. 9 Magnetic moment in both ferromagnetic and super paramagnetic materials (Mody et al., 2013).

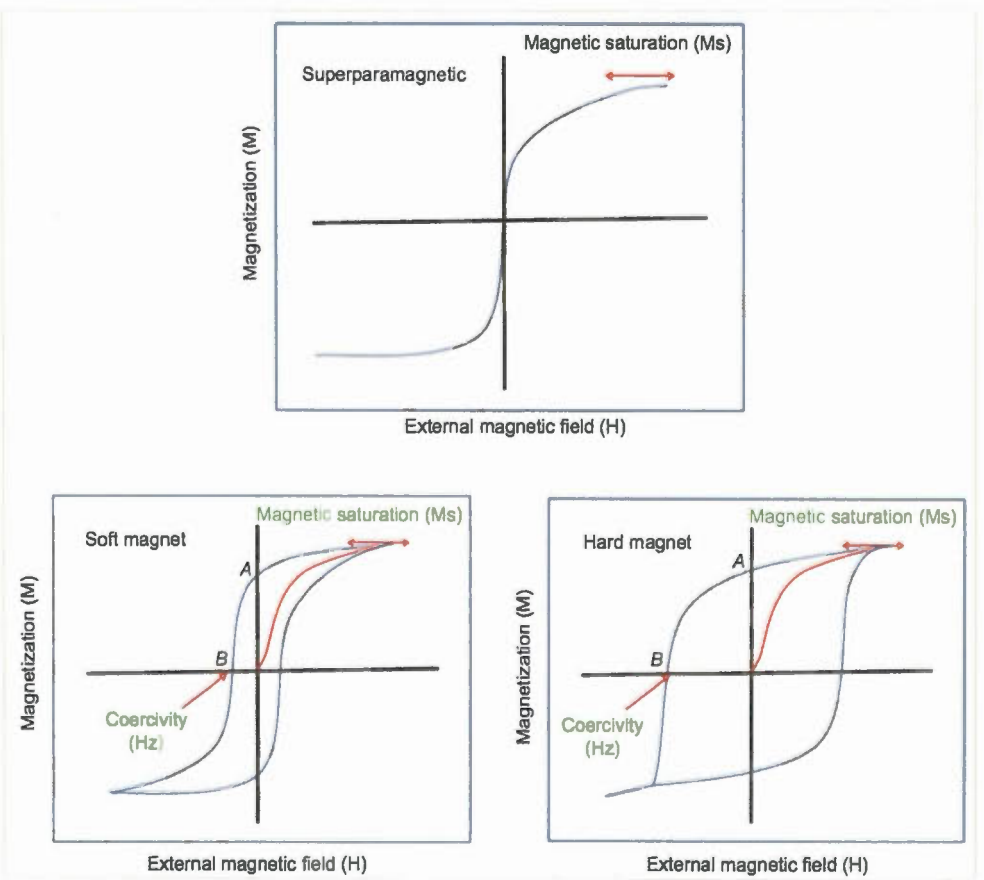

Figure 1. 10 A typical hysteresis loop such as that obtained from super paramagnetic and ferromagnetic (soft and hard) materials (Mody et al., 2013)

1.5 Nanoparticles synthesis Methods

They're many different approaches of producing nanoparticles. First very rough classification scheme is to separate them into top-down and bottom-up approaches. On top down approaches, the source material is reduced from bulk size to nanoscale scale as in attrition processes (e.g., grinding). Grinding is a mechanical attrition process, which operates on the solid phase. Bottom-up processes can be further subcategorized into vapor phase (e.g, pyrolysis, inert gas condensation), and liquid phase (e.g., solvothermal, sol-gel) fabrication. A generic visualization of these two-phase methods is provided in Figure 1.11 (Overney, 2010).

Up to now, there are several methods that can use to synthesize iron carbide based nanomaterials. These methods include Arc Discharge Plasma (ADP) method, Laser ablation synthesis, and Chemical Vapour Deposition. Herein, we follow the synthesis method, which used to generate carbon nanostructures, such as Multi-Walled Carbon Nanotubes (MWCNT). We focus on vapor phase fabrication to produce carbon-shell FeC@Graphene nanoparticles.

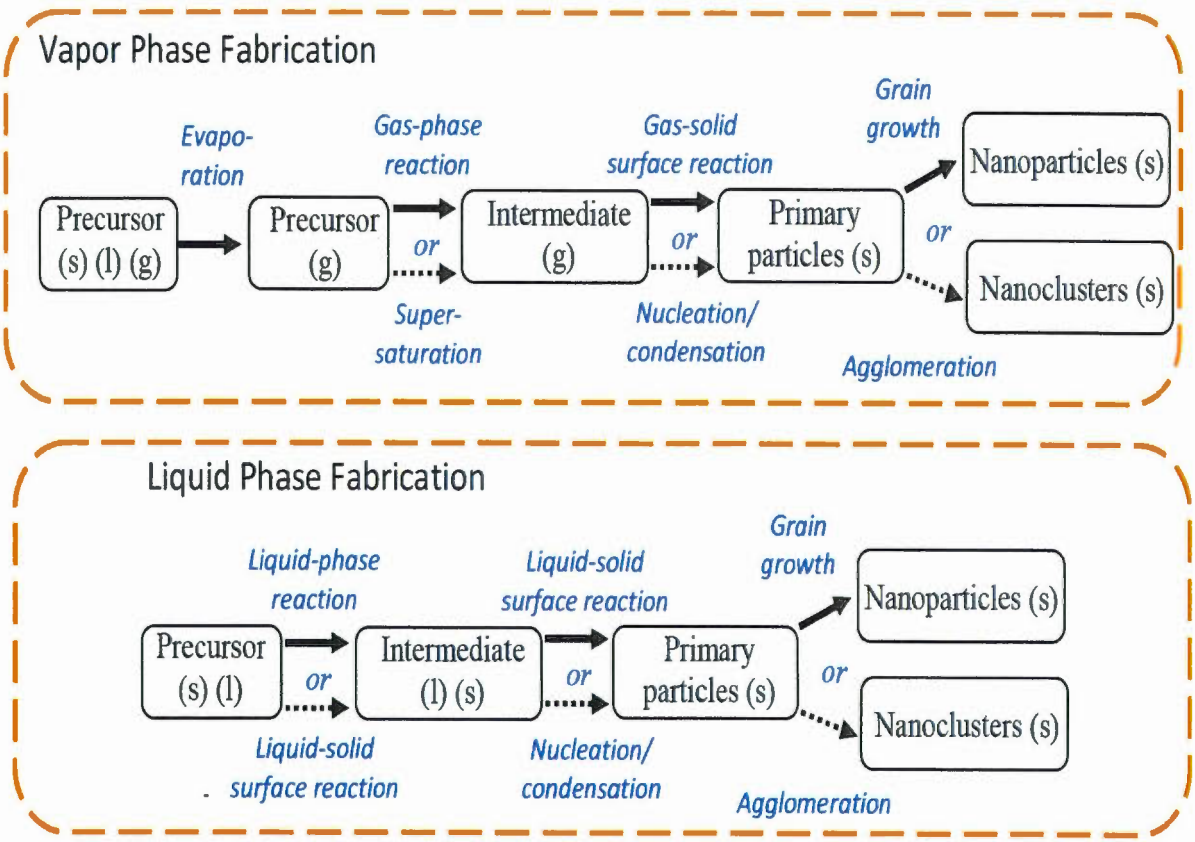

Figure 1. 11 Generic concepts of bottom-up nanoparticle fabrication processes based on the phase in which the particles were formed (Overney, 2010).

1.5.1 Arc Discharge Plasma (ADP) method

Carbon-encapsulated magnetic Fe nanoparticles with low carbon content have been produced via an arc discharge process in ethanol vapor (Si et al., 2003). A schematic diagram of the arc discharge apparatus is shown in Figure 1.12.

In this method, two graphite electrodes are installed vertically, and the distance between the two-rod tips is usually in the range of 1 - 2 mm. The anode and cathode are made of pure graphite (those are, with a purity of 99.999%). The anode is drilled, and the hole is filled with a mixture of catalysts metal powder then the chamber is connected to a vacuum line with a diffusion pump and to a gas supply. To decrease the large amount of unwanted carbonaceous debris produced, a tungsten cathode instead of a carbon one was used. However, encapsulated nanocrystal were generated, mixed together with encapsulated nanocrystal and a small amount of carbonaceous debris (Jahanshahi & Kiadehi, 2013) (Si et al., 2003).

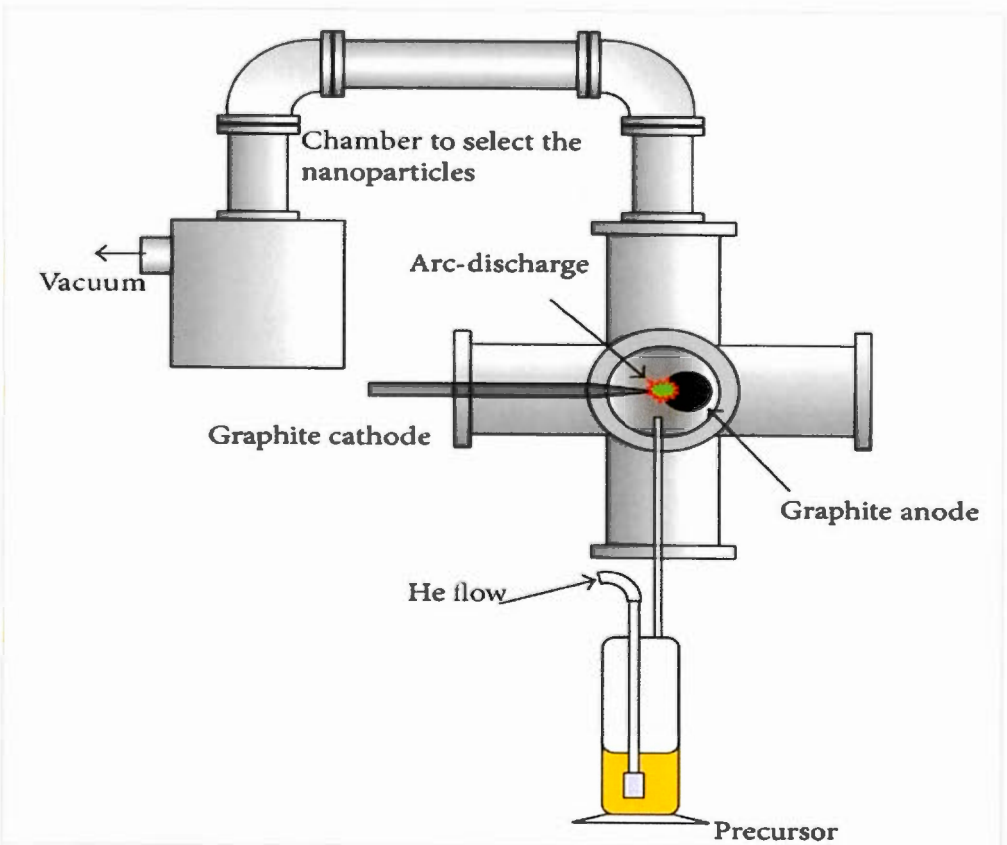

Figure 1. 12 General picture of the "home made" reactor used for the synthesis of the iron encapsulated in carbon nanoparticles (Chaitoglou, Sanaee, & Bertran, 2014).

1.5.2 Laser ablation synthesis

The application of laser irradiation to ablate materials from a target was firstly reported in the early 1960s when the ruby lasers became available (Yang, 2007). Pulsed laser ablation in aqueous media has provided a new technique for synthesis of size controlled metallic nanoparticles and provided a powerful tool for the synthesis of nanomaterials in both solutions and gas matrices (S. C. Singh & Gopal, 2007).

The conventional method for producing metal or metal compound nanoparticles is laser ablation of a metal in a solvent. The laser ablation synthesis in solution (LASiS) approach for the synthesis of magnetic nanoparticles has a strength point in the basic experimental set-up, which requires a minimum manual operation. It consists of a pulsed laser, a set of focusing optics and a vessel containing the metal plate, which is placed in proximity of the focus Figure 1.13 (Amendola & Meneghetti, 2009).

The principle of the laser-based synthesis of iron in an organic solvent (pentane, hexane, or decane) performed using an airtight cell to produce iron carbide nanoparticles. Most experiments involving laser ablation in solvents employ open-air conditions in which the target material is placed at the bottom of a vial filled with a solvent and the surface of the solvent is in contact with air. When laser light is irradiated through the surface of the solvent to the Fe metal sample at the bottom of the glass vial, and the target material is vaporized and condenses in the solvent thus forming nanoparticles, bubbles produced by laser ablation disturb the surface,

destabilizing the focal point and causing iron oxide to be produced because of dissolved air in the solvent. Therefore; an airtight cell designed to perform laser ablation under stationary conditions in inert gas atmosphere and to prevent the nanoparticles from being oxidized. A convex lens was directly attached to the side of the cell contacting the liquid and Ar gas was used to fill the space at the top of the cell (Matsue, Yamada, & Kobayashi, 2012) (Wagener, Barcikowski, Bärsch, & Gmbh, 2011). The nanoparticle sizes depend on both the laser influence and the nature of the liquid. In some cases, nanoparticles of compounds are formed via the reaction of the metal with the liquid (Dolgaev, Simakin, Voronov, Shafeev, & Bozon-Verduraz, 2002).

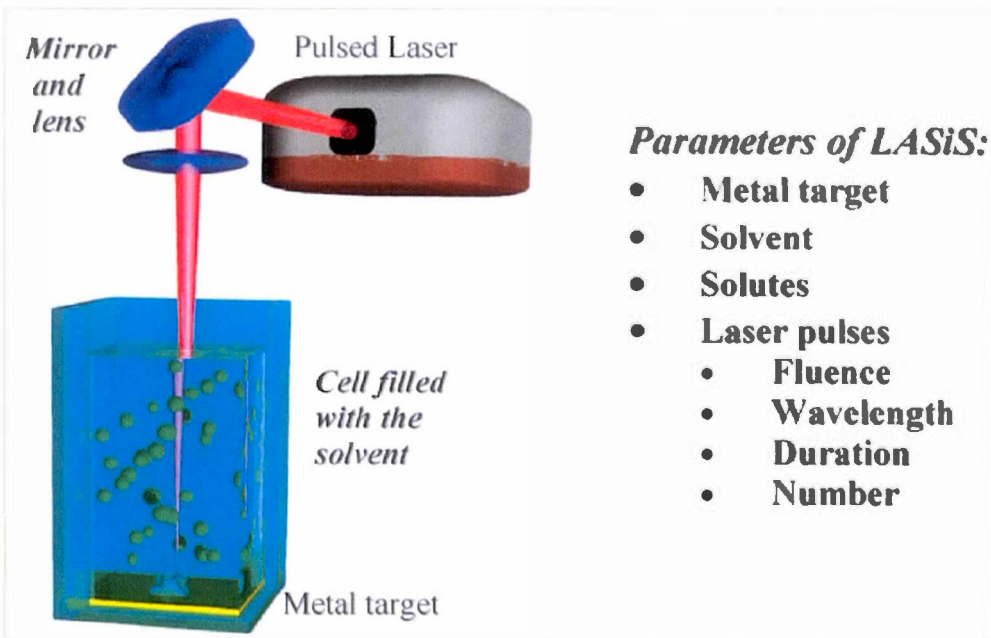

Figure 1. 13 The principal components of the experimental set up for LASIS with a list of its main parameters (Amendola & Meneghetti, 2009).

1.5.3.Chemical Vapour Deposition (CVD)

1.5.3.1 Definition

Chemical Vapour Deposition (CVD) involves the dissociation and/or chemical reactions of gaseous reactants in an activated (heat, light, plasma) environment, followed by the formation of a stable solid product. The deposition involves homogeneous gas phase reactions, which occur in the gas phase, and/or heterogeneous chemical reactions, which occur in/near the vicinity of a heated surface leading to the formation of powders or films, respectively (Choy, 2003).

1.5.3.2 CVD system

Among these methods, chemical vapour deposition (CVD) using transition metal substrates has been considered the most promising, inexpensive and feasible method to produce a single layer or multi-layers graphene. CVD using Cu is one of the fastest developing processes to produce single layer graphene due to the low solubility of carbon in Cu, which leads to a self-limited process. It has been shown that large area of graphene could be obtained and excellent device properties can be achieved by this method. Figure 1.14 demonstrates a schematic of an experimental setup of CVD coating. It basically consists of a tube furnace for high temperature heating, a quartz vacuum chamber, a vacuum and pressure control system for the growth conditions

adjustment, and several mass flow controllers (MFC) to provide carbon source and reactant gases with a necessary flow rate (Kumar & Lee, 2013).

The growth nanoparticles mechanisms in the CVD process have been generally divided into two distinct methods. First, typical CVD process (i.e. using Cu as a substrate) involves dissolving carbon into the substrate followed by a precipitation of carbon on the substrate by cooling the substrate. The substrate is placed in a CVD chamber at a vacuum of 10^4 Torr and temperature below 1000°C. After the furnace is heated to the appropriate reaction temperature, a flow of gaseous carbon precursor is introduced for a given time period. The deposition process starts with the incorporation of a limited quantity of carbon atoms into the substrate at relatively high temperature. The subsequent rapid quenching of the substrate caused the incorporated carbon atoms to out-diffuse onto the surface of the substrate and form graphene layers. Then, the magnetic material is introduced in the controlled-temperature furnace in a liquid, gas or solid state and decomposes; and heating periods can reach several hours.

1.5.3.3 Temperature

Generally, the growth temperature is between 550 °C and 1200 °C, and the reaction temperature may vary according to the catalyst-support material pair. General experience is that low temperature CVD (600 - 900 °C) yields MWNTs, whereas higher temperature (900 - 1200°C) reaction favors SWNT growth indicating that the

latter have a higher energy of formation. The reaction temperature also plays an important role in the alignment properties and diameter of the synthesized partial. Within the temperature range of 600-900°C, diameter distribution of MWNTs increases with the increasing temperature. The lower is the CVD temperature the narrower is the diameter distribution (Cnms, Bhattacharjee, & Nath, 2012).

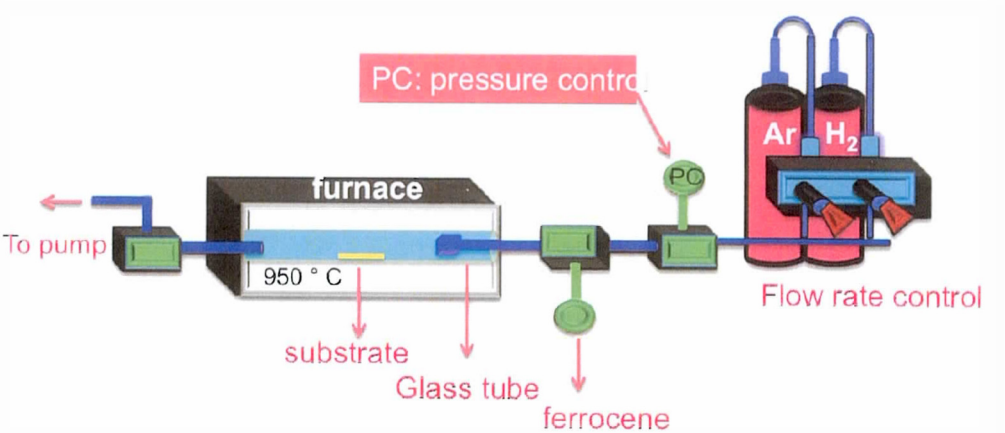

Figure 1. 14 Schematic diagram of a common setup for chemical vapour deposition of core-shell NPs (M.Alahmadi, 2016).

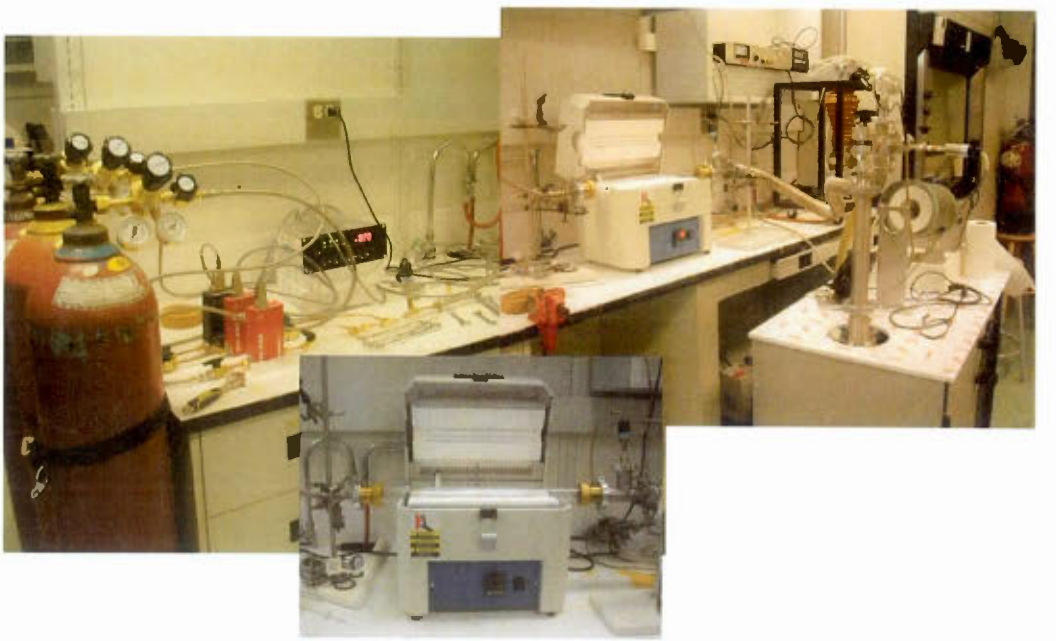

Figure 1. 15 Photo of a CVD deposition system (M.Alahmadi, 2016)

1.6 Application of FeC@Graphene NPs

There are a number of potential applications for magnetic FeC@Graphene nanoparticles, in terms of medical applications and electrical applications.

1.6.1 Potential medical applications

The use of magnetic nanoparticles in medical applications is a novel and highly interdisciplinary field offering great potential in therapeutic and diagnostic testing, in vitro and in vivo (Vatta, Sanderson, & Koch, 2006). They have controllable sizes ranging from a few nanometers up to tens of nanometers, which places them at dimensions that are smaller than or comparable to those of a cell (10 – 100 μm), a

virus (20 – 450 nm), a protein (5–50 nm) or a gene (2 nm wide and 10 –100 nm long). This means that they can 'get close' to a biological entity of interest. Indeed, they can be coated with biological molecules to make them interact with or bind to a biological entity, thereby providing a controllable means of 'tagging' or addressing it. The nanoparticles are magnetic, which means that they obey Coulomb's law, and can be manipulated by an external magnetic field gradient. This 'action at a distance', combined with the intrinsic penetrability of magnetic fields into human tissue, opens up many applications involving the transport and/or immobilization of magnetic nanoparticles, or of magnetically tagged biological entities. In this way they can be made to deliver a package, such as an anticancer drug, or a cohort of radionuclide atoms, to a targeted region of the body, such as a tumour (Pankhurst, Connolly, Jones, & Dobson, 2003).

One of the main envisaged therapeutic applications of coated magnetic nanoparticles is for targeted chemotherapeutic drug delivery to tumors. Particles coated with a drug could be injected intravenously, transported to a site of action (e.g., cancerous tumor or arterial blockage) and be retained at the site by the application of a magnetic field gradient.

A second important therapeutic application is in the field of hyperthermia, which involves heating organs or tissues between 41 and 46 °C to obtain tumor cell necrosis. The application of an external alternating magnetic field to nanosized magnetic particles causes heating via hysteresis energy losses (Vatta et al., 2006).

Super paramagnetic nanoparticles are used as magnetic resonance imaging (MRI) contrast agent in diagnostic applications. MRI may be used to enhance the image contrast between normal and diseased tissue and/or indicate the status of organ functions or blood flow. Medical applications require particles with high saturation magnetization, exhibiting super paramagnetic behavior and small enough to interact in the region of interest, e.g., to promote tissular diffusion (Vatta et al., 2006) (Häfeli, 2004).

1.6.2 Electrical applications

To date, the largest practical application of iron nanoparticles is in the realm of magnetic recording media, where high coercivity is critical. On the other hand, in transformer core materials, very low coercivity is desirable. Currently, the largest commercial application of carbon encapsulate iron nanoparticles is using them as magnetic recording media. Many advanced magnetic tapes, such as those used in computer backup tapes and camcorders achieve their very high capacity through the use of iron nanoparticles (Huber, 2005).

CHAPTER II

NANOTOOLS

In this chapter, details about various important analysis techniques, which have been used to characterize products, are reported. The main techniques that have been used are Transmission Electron Microscopy (HRTEM, TEM), Scanning Electron Microscope (SEM), Energy Dispersive X-ray Microanalysis (EDX), Superconducting Quantum Interference Device (SQUID), and Raman spectroscopy. In this chapter, we provide a brief introduction of the principle operating of these techniques. Moreover; studying the magnetic properties of nanoparticles is performed.

2.1 Electron Microscope (EM)

Electron Microscopes are scientific instruments that use a beam of highly energetic electrons to examine objects on a very fine scale. This examination can yield information about the topography (surface features of an object), morphology (shape and size of the particles making up the object), composition (the elements and compounds that the object is composed of and the relative amounts of them) and crystallographic information (how the atoms are arranged in the object). Electron Microscopes were developed due to the limitations of Light Microscopes, which are

limited by the physics of light to 500x or 1000x magnification and a resolution of 0.2 micrometers. In the early 1930's this theoretical limit had been reached and there was a scientific desire to see the fine details of the interior structures of organic cells (nucleus, mitochondria...etc.). This required 10,000x plus magnification, which was just not possible using Light Microscopes (Stefanaki, 2008).

Several different types of electron microscopes exist. Two major ones include the transmission electron microscopy (TEM) and the scanning electron microscopy (SEM). Electron microscopes function exactly as their optical counterparts except that use a beam of high-energy electrons to probe the sample. Electron microscopy is a scientific instrument that uses a beam of highly energetic electrons to examine objects on a very fine scale. The principal works, and the theory of electron-specimen interaction of different types of EMs are described in more detail below (John F. Mongillo, 2007).

2.1.1 Scanning Electron Microscope (SEM)

Scanning Electron Microscope (SEM) can provide information about surface topography, crystalline structure, chemical composition and electrical behavior of the top 1 um or so of samples. Various specialized stages such as hot, cold or designed to permit in situ mechanical testing can be attached to enable behavior under various conditions to be examined. SEM magnifies an electron beam that is produced by a source gun see Figure 2.1a. After acceleration towards the anode, one or two

condenser lenses focus them. The electron beam also passes through pairs of scanning coils, which deflect the beam in the x and y directions, so that it scans in a raster mode over a rectangular area of the sample surface. The interaction between the specimen and the electron beam produces various types of emissions, which are captured by various detectors, placed in appropriate positions. Morphological/ topological-contrast and compositional information are separately obtained by selecting specific types of emitted electrons, known as secondary electrons (SEs-with energies smaller than 50 eV) and backscattered electrons (BSE-with energies larger than 50 eV), respectively. Further compositional information is obtained through the detection of characteristic X-rays using an X-ray detector (Suga et al., 2014) (Reithmeier, Vynnyk, & Schultheis, 2010).

2.1.2 Specimen preparation

For semiconductors, no special specimen preparation is required. The surface to be examined is ply specifically to semiconductor mounted on a special SEM stub with electrically conducting pads. If the specimen is mounted on an insulator then to prevent the specimen from charging (which distorts the image) a conduction path to ground is required. If EBIC or volt- age contrast is being used, then suitable electrical connections are also required.

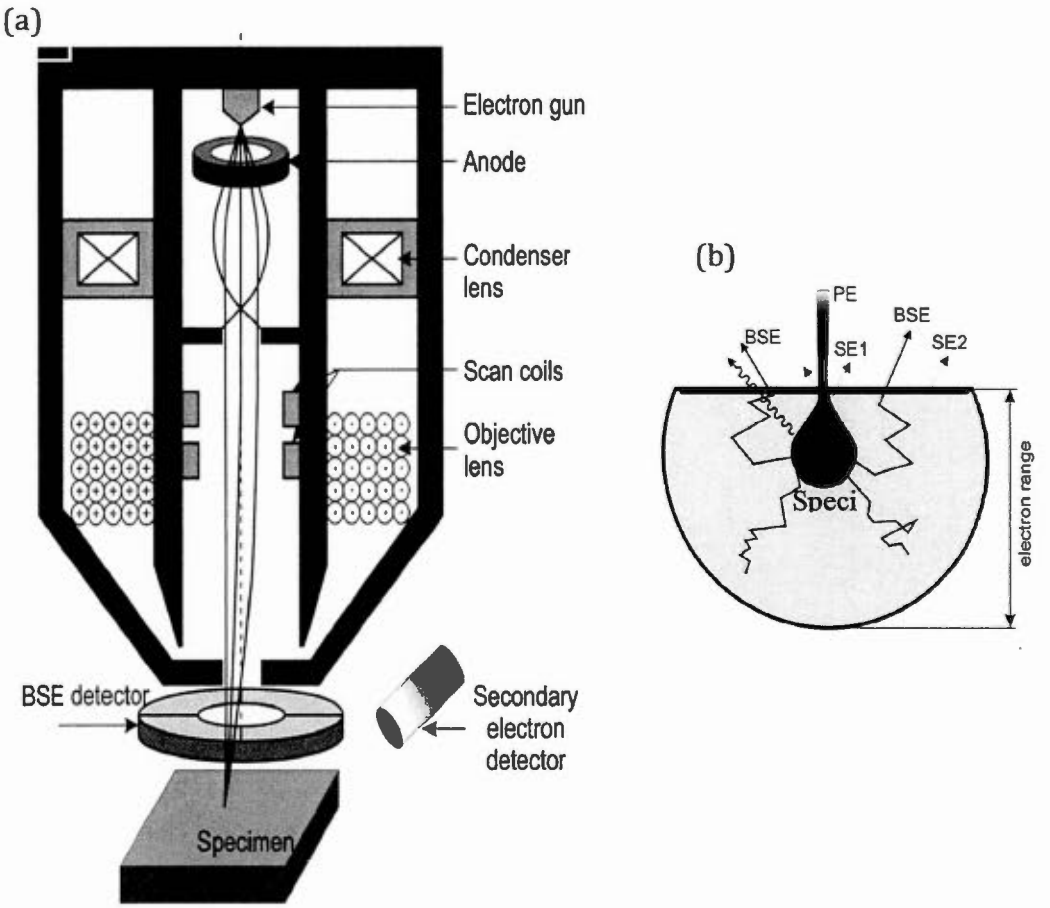

Figure 2. 1 Basic depictions of (a) Schematic diagram of SEM, (b) introduction volume (Reithmeier et al., 2010)

2.2 Transmission Electron Microscopy (HRTEM, TEM)

TEM is a versatile tool that provides not only atomic-resolution lattice images, but also chemical information at a spatial resolution of 1 nm or better, allowing direct identification the chemistry of a single nanocrystal. A schematic drawing of the TEM equipment is shown in Figure 2.2. A modern TEM is composed of an illumination system, a specimen stage, an objective lens system, the magnification system, the data recording system, and the chemical analysis system. The electron gun is the heart of the illumination system, which typically uses LaB_6 thermionic emission source or a field emission source. The illumination system also includes the condenser lenses that are vitally important for forming a fine electron probe. The specimen stage is key to carrying out structure analysis, because it can be used to perform in situ observations of phenomena induced by annealing, electric field, or mechanical stress, giving the possibility of characterizing the physical properties of individual nanostructures. The objective lens is the heart of a TEM, which determines the limit of image resolution. The magnification system consists of intermediate lenses and projection lenses, and it gives a magnification up to 1.5 million. The data recording system tends to be digital with the use of a charge-coupled device (CCD), allowing quantitative data processing and quantification. The data recording system tends to be digital with the use of a charge-coupled device (CCD), allowing quantitative data processing and quantification. Finally, the chemical analysis system is the energy-dispersive X-ray spectroscopy (EDS) and electron energy loss spectroscopy (EELS),

both can be used complementary to quantify the chemical composition of the specimen (Wang, 2000) (Rai & Subramanian, 2009).

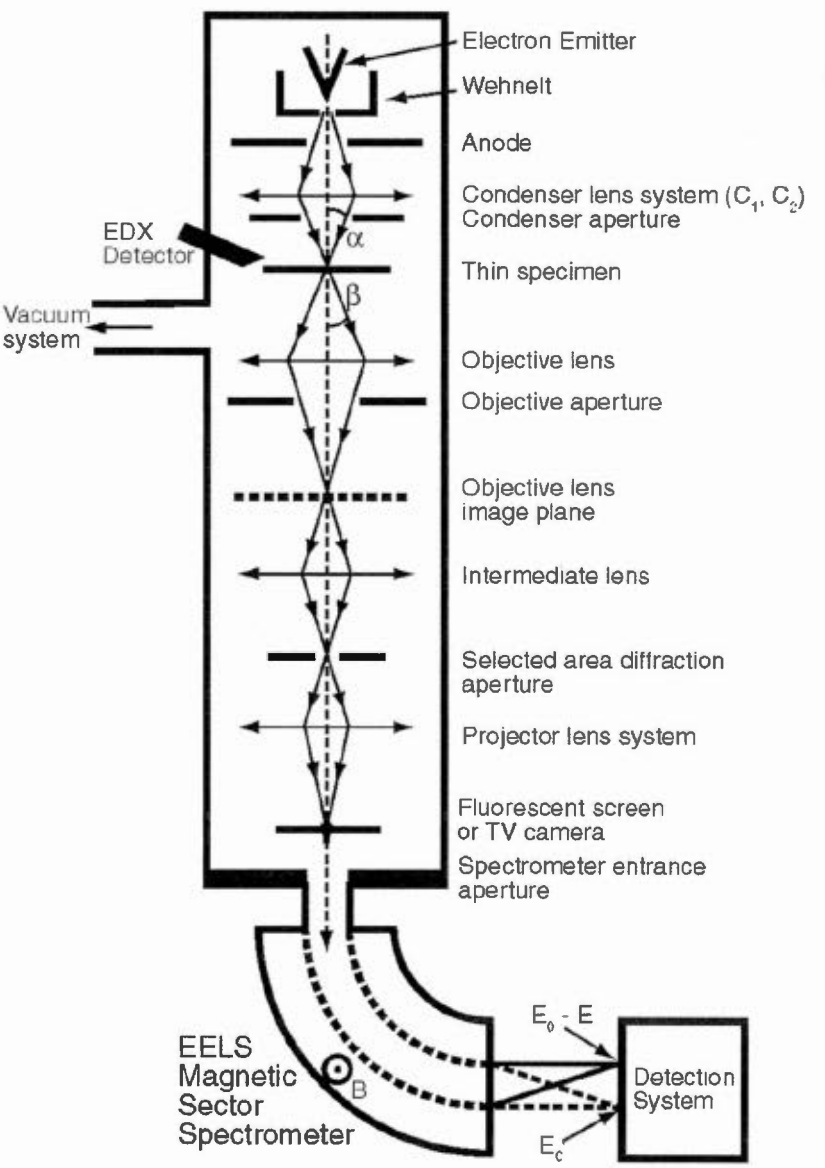

Figure 2. 2 Schematic diagram of the layout of an analytical conventional transmission electron microscope (Rik Brydson1, Andy Brown1, 2005)

2.3 Energy Dispersive X-ray Microanalysis (EDX)

Energy Dispersive Spectroscopy (EDS, also sometimes called EDX or Energy Dispersive X-ray Analysis) is the most frequently used chemical analysis tool in failure analysis. It has some very significant advantages. It is used as an attachment to the SEM (Scanning Electron microscopy), which is readily available in every failure analysis laboratory. Analysis is performed in minutes, the spectra are easily interpreted, and spatial resolution is good. While much of the EDS work is performed in SEM, EDS system also function on TEM (Transmission Electron Microscope), with some significant advantages in terms of interaction volume. The chractrasation X-ray generation process Figure 2.3 is initial with the ejection of an inner shell electron to form a vacancy. From this excited state, an electron from the outer shell jump into the vacant site for filling the inner shell. During this process, the sample fluoresces X-ray of energy same as the energy difference between the initial state and final state. Since each atom has its unique and discretized energy levels, the x-Ray fluorescence is also characteristic of that atom. Energy dispersive X-ray spectroscopy is a technique that detects the x-ray fluorescence to characterize the elements present in a material. The nomenclature for various X-ray generated is as following. The initial nomenclature is taken from electronic shell of the initial vacancy created by the electron using K, L, M and N as shell name. These letters are used the designate the number of shells above the vacancy from which replacing electron falls α, β, γ, δ Figure 3.3 (Wagner, 1999).

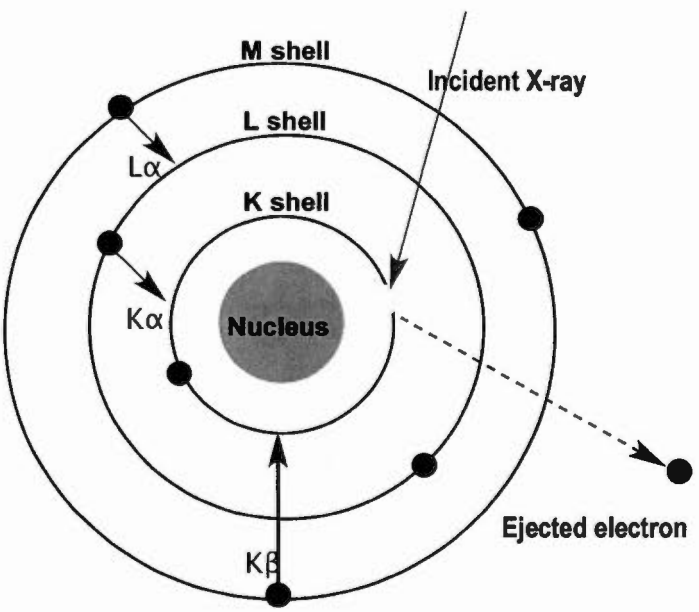

Figure 2. 3 Schematic diagram shows of energy dispersive X-ray spectroscopy (EDX). In EDX, in incoming X-ray ejects an inner shell electron, leaving a vacancy, which is filled by an outer shell electron, releasing a photon (M.Alahmadi, 2016).

2.4 Selected Area Electron Diffraction (SAED)

SEAD is the most popular diffraction technique in TEM. The technique can be applied to study both crystalline and noncrystalline structures. The large area illumination is useful for recording diffraction patterns from polycrystalline samples or averaging over a large volume (e.g., al large number of nanoparticles). SAED can also be used for low-does electron diffraction, which is required for studying radiation sensitive materials, such as organic molecules (Scott, 2007).There are tow fundamentally distinct methods of forming an electron diffraction pattern. The ray diagram in Figure 2.4 shows the formation of so-called selected area diffraction (SAED) pattern in transmission electron microscopy. A nearly parallel electron beam is an incident on the specimen and a regular array of diffraction spots is formed by transmission of the electron beam through a single thin crystal. To reduce the specimen area contributing to the diffraction pattern, an aperture in the image plane conjugate to the specimen plane is inserted. Ideally, if the diameter of the aperture is D and the magnification of the objective lens is M, the affective diameter of the area selected on specimens should be equal to D/M. However; the spherical aberration of the objective lens as well as its focus error makes it impossible to reduce the size of the selected area beyond a certain limit, so in practice the resolution of the technique is limited and typically is not less than several hundred nanometers (Peng, Dudarev, & Whelan, 2005).

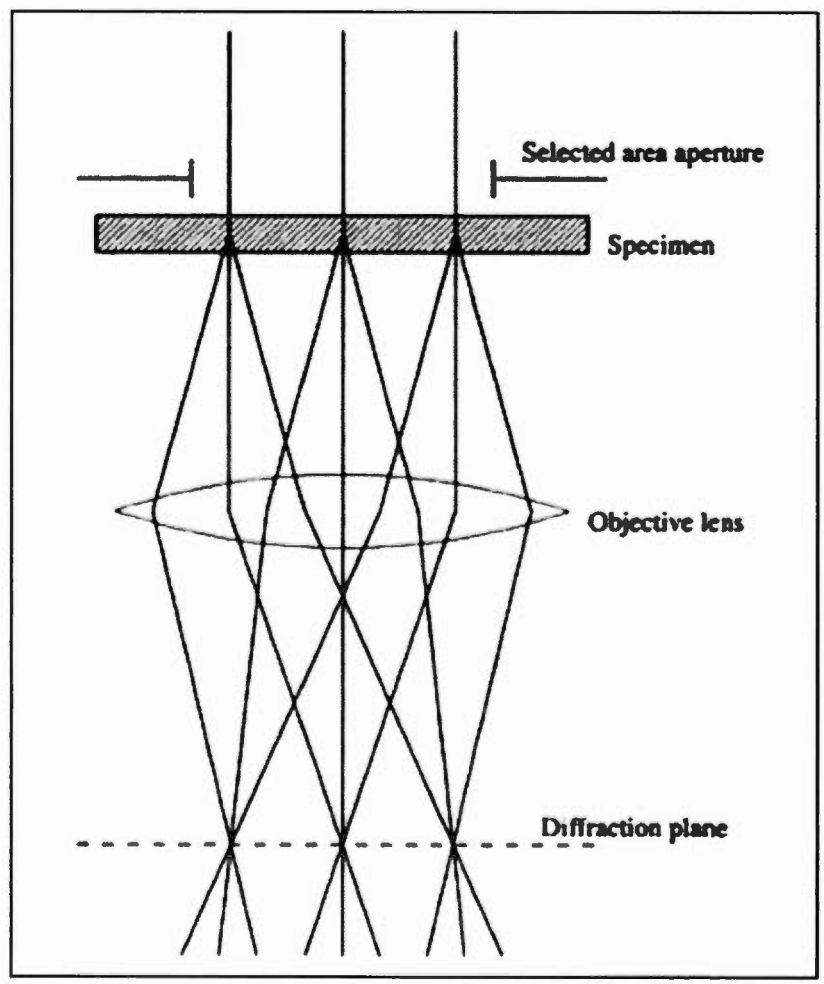

Figure 2. 4 Schematic diagram shows the principles of the formation of SAED. The selected area aperture in the figure is an effective or virtual one. The real selected area aperture is in a plane, which is not shown in the figure (Peng et al., 2005).

2.5 Superconducting Quantum Interference Devices: SQUID

SQUID "Superconducting Quantum Interference Devices" are the most sensitive devices in detecting the magnetic flux. For the present work, SQUID have been used to detect small magnetic field and magnetic susceptibility. A SQUID consists of a superconducting ring interrupted by one or two Josephson junctions. The single junction SQUIDs is also known as RF-SQUIDs the junction is shorted by superconductor path; therefore the voltage response obtain by coupling the loop to a RF bias tank circuit. The double junction SQUIDs is also known as DC-SQUIDs. In this device the two weak links are not shorted by superconductor path; therefore the DC current-voltage characteristics can be observed. This device applies current who slightly greater than the critical current and one can monitor the voltage drop across the device (Aviv, 2008) (Greenberg, 1998).

SQUID magnetometers or susceptometer (MS) can be readily optimized to measure the induced or remnant magnetic moment in a sample depends on applied magnetic field and temperature. To make a measurement, a sample, typically less than a few millimeters in size, is first attached to a sample rod. The sample is then scanned through the center of a first- or second-order superconducting gradiometer (see Figure 2.5). The gradiometer forms a closed flux transformer that is coupled to a SQUID and the signal from the SQUID is typically recorded as a function of sample position. The shape and magnitude of the response curve can then be analyzed using a computer to

obtain a corresponding magnetic moment. To apply a magnetic field to the sample, the detection coils are located in the bore of a superconducting magnet. Temperature control is made possible by placing the sample and sample rod in a sealed variable-temperature insert (not shown in Figure 2.5) which is thermally isolated from the 4.2-K gradiometer and magnet by an annular vacuum space (Black & Wellstood, 2006).

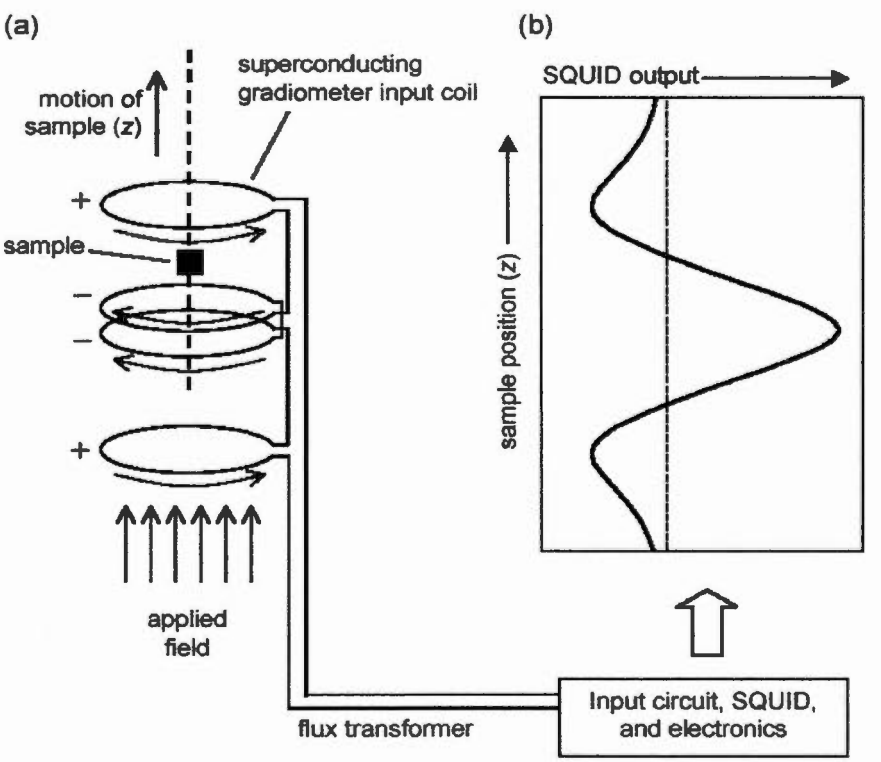

Figure 2. 5 (a) Schematic of SQUID magnetometer–susceptometer, (b) Calibrated output from SQUID electronics, recorded as a function of position (Black & Wellstood, 2006).

2.6 Raman Spectroscopy

Raman spectroscopy provides chemical structural information at molecular level with minimal sample preparation in a quick, easy-to-operate and reproducible fashion.

2.6.1 Raman scattering

The Raman effect can be described as an inelastic light scattering process. When a strong light source (laser) is focused on a substance, most of this energy will be scattered elastically. Two types of scattering are readily identified. The most intense form of scattering, Rayleigh scattering, occurs when the electron cloud relaxes without any nuclear movement. This is essentially an elastic process and there is no appreciable change in energy. Raman scattering, on the other hand, is a much rarer event, which involves only one in 10^6–10^{10} of the photons scattered. This occurs when the light and the electrons interact and the nuclei begin to move at the same time. Since the nuclei are much heavier than the electrons, there is an appreciable change in energy of the molecule to either lower or higher energy depending on whether the process starts with a molecule in the ground state (Stokes scattering) or from a molecule in a vibrational excited state (anti-Stokes scattering). Figure 2.6 shows a simple diagram illustrating Rayleigh and Raman scattering. In each case the energy of the virtual state is defined by the energy of the incoming laser. The two states marked m and n are different vibrational state-of-the-ground electronic state (Edwards, 2005).

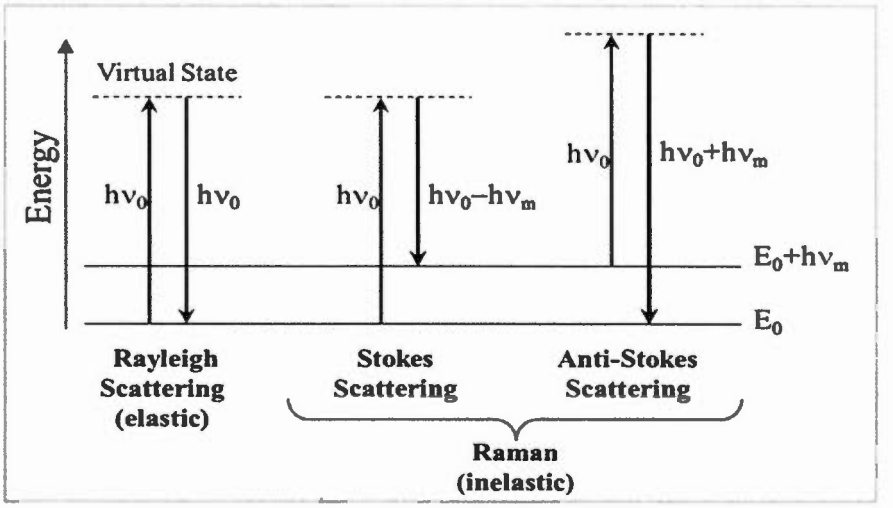

Figure 2. 6 Diagram of the Rayleigh and Raman scattering processes (Smith, Dent, & Wiley, 2013)

2.6.2 Raman spectrum of graphene and graphene layers

Different types of carbon nanostructures including; multi-walled nanotubes (MWNT), double-walled carbon nanotube (DWCNT), single-walled carbon nanotubes (SWCNT), and NPs consists of two characteristic bands in Raman spectra, namely, the G-band at 1583 cm^{-1} and the at G' 2700 cm^{-1}. Comparing Raman spectra of graphene and graphite show some significant differences as we can see in Figure 2.7. The most obvious difference is that the band at 2700 cm^{-1}, which is known as the G' band, is much more intense than the G band in graphene compared to graphite. You may have heard the G' band referred to as the 2D band; both 2Dand G' are accepted names for this band. Also, figure shows a significant change in the shape and intensity of the G' peak of graphene compared to bulk graphite. The G' peak in

bulk graphite consists of two components $2G'_1$ and $2\ G'_2$, roughly 1/4 and 1/2 the height of the *G* peak, respectively. Graphene has a single, sharp G' peak, roughly four times more intense than the *G* peak. Closer look at the G' band of these two materials, we can see that both the shape of the band and the position are different Figure 2.8. The peak shift in graphite is a result of interactions between the stacked graphene layers, which has a tendency to shift the bands to higher frequency. Figures 2.8b and 2.8c show the same spectra as in Figure 2.8a with the addition of curve fitting. The G' band in a single layer graphene spectrum fits to a single band whereas curve fitting reveals several underlying bands in the graphite spectrum (Ferrari, 2007) (Hodkiewicz, 210AD).

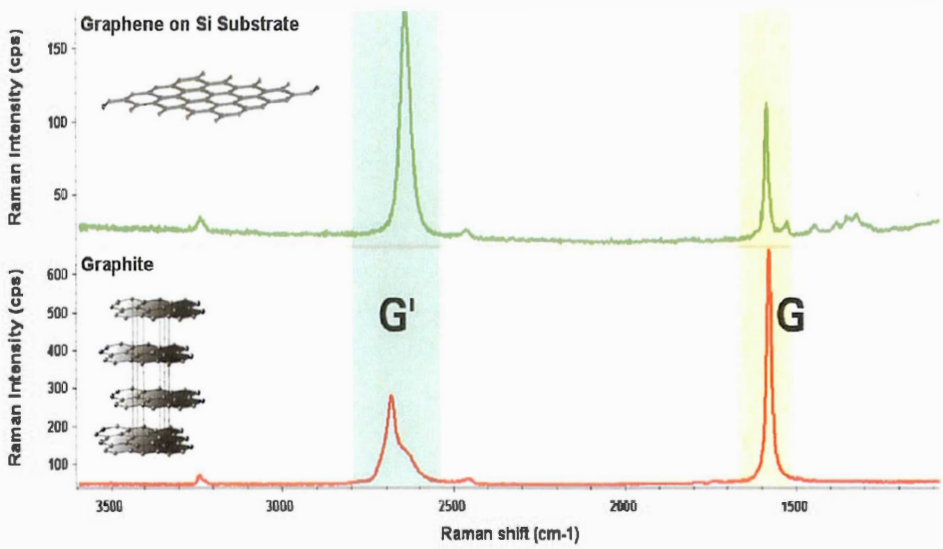

Figure 2. 7 Comparison of Raman spectra of graphene and graphite (Hodkiewicz, 210AD)

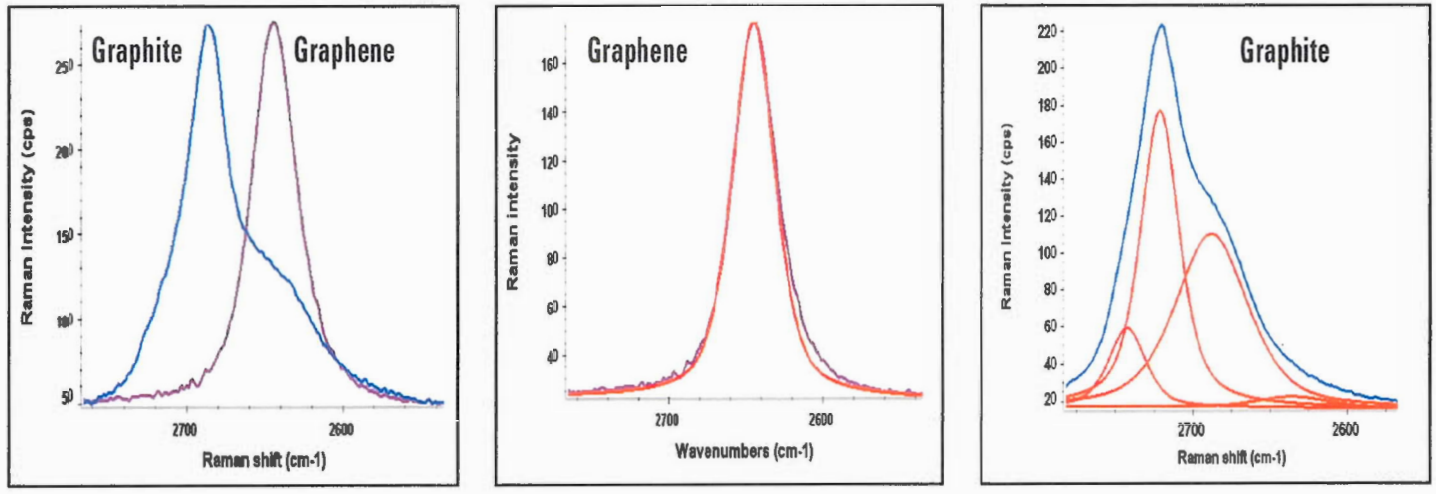

Figure 2. 8 (A) G' band of graphite and graphene (B) G' band of graphene with curve fitting (C) G' band of graphite with curve fitting (Hodkiewicz, 210AD)

2.7 X-Ray Diffraction

X-ray diffraction (XRD) is an analytical technique looking at X-ray scattering from crystalline materials. Each material produces a unique X-ray "fingerprint" of X-ray intensity versus scattering angle that is characteristic of it's crystalline atomic structure. Qualitative analysis is possible by comparing the XRD pattern of an unknown material to a library of known patterns (Knipping & Laue, 1952).

2.7.1 Instrumentation

The mechanical assembly that makes up X-ray source, sample holder, detector arm and associated gearing is known as Goniometer Figure 2.9. The X-ray is focused on the sample at some angle θ, while the detector opposite the source reads the intensity of the X-ray it receives at 2θ away from the source path. The 2θ values for the peak depend on the wavelength of the anode material of the X-ray tube. Hence, it becomes necessary to reduce peak position to the interplanar spacing ***d*** that corresponds to the ***h, k, l*** planes that caused the reflection. The value of the ***d*** spacing depends only on the shape of the unit cell. The ***d*** spacing is obtained as a function of 2θ from Bragg's law. From the values of the d spacing and the corresponding index ***h, k, l*** the dimension of the unit cell can be calculated (Bhowmick, 2012).

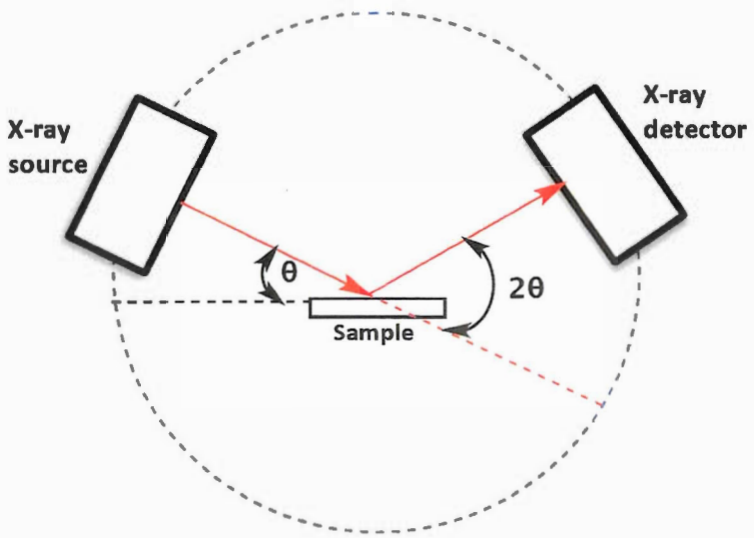

Figure 2. 9 Schematic representation of a powder X-ray diffraction (M.Alahmadi, 2016)

2.7.2 Bragg's law

Figure 2.9 is the construction needed to derive Bragg's law. The angle of incidence of the two parallel X-ray is θ. We can prove that the small angle in the little triangle is equal to θ by showing that the two right triangles, ABC and ACD, are similar. The interplanar spacing, ***d***, sets the difference in path length for the ray scattered from the top plane and the ray scattered from the bottom plane. Figure 2.10 shows that this difference in path lengths is ***2d sin θ***. Constructive wave interference (and hence strong diffraction *n*) occurs when the difference in path length for the top and bottom rays is equal to one wavelength, λ:

$$2d \sin \theta = n\lambda$$

Where θ is the angle of incidence of the X-ray, n is an integer; λ is the wavelength,

and ***d*** is the spacing between atoms layers(Fultz & Howe, 2007).

2.7.3 Sample preparation

X-ray diffraction can be done on a number of different kinds of sample, normally it distinguishes between single crystal and polycrystalline or powder applications. The single crystal sample is a perfect (all unit cells aligned in a perfect extended pattern) crystal with a cross section of about 0.3 mm. In powder or polycrystalline diffraction it is important to have a sample with a smooth plane surface. If possible, we normally grind the sample down to particles of about 0.002 mm to 0.005 mm cross section. The ideal sample is homogeneous and the crystallites are randomly distributed. The sample is pressed into a sample holder so that we have a smooth flat surface (To, 1999).

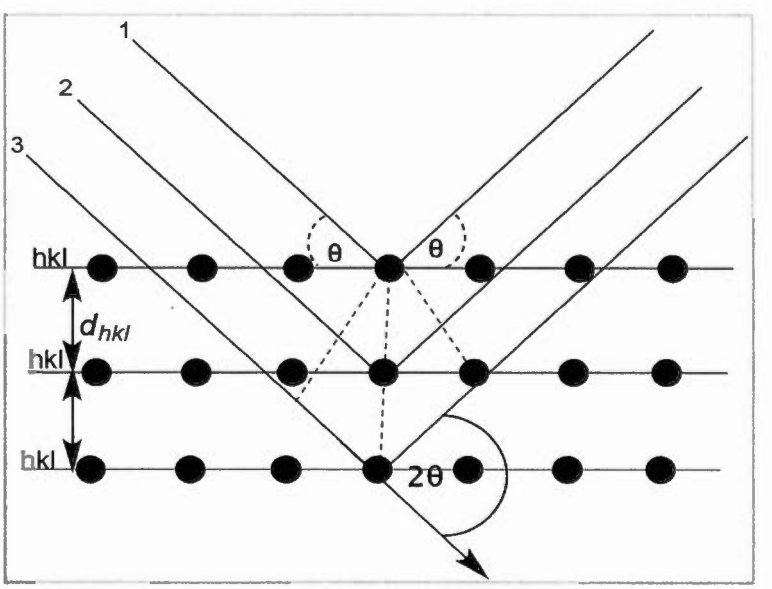

Figure 2. 10 Deriving Bragg's Law using the reflection geometry and applying trigonometry (M.Alahmadi, 2016).

CHAPTER III

SYNTHESIS OF FEC MAGNETIC NANOPARTICLES

This chapter will highlight on the description a method to synthesis nanoparticles with graphene shells by chemical vapor deposition (CVD) using ferrocene metal powder as the starting material and the formation process are reported. All the process steps starting from the substrate preparation to the transfer product are described in detail. Also, in this section, a one-step synthesis methodology to prepare different sized of nanoparticles encapsulated with graphene sheets will be presented. A detailed characterization of the magnetic nanoparticles will also be explained.

3.1 Synthesis FeC@Graphene NPs

The experimental procedure for growth FeC@Graphene NPs begins with cleaning cupper foils (Cu) to be used as a catalyst. The copper foil material was cut approximately 1×1 cm^2 sized and immersed in several solvents (Acetone for 10 min followed by immersion in Nano-water for 10 min and Isopropyl alcohol (IPA) for 10 min) in order to clean it before the insertion into the furnace. The cupper foils were then loaded into two-inch quartz tube. Often many copper foils loaded for single run.

When all the foils were loaded, the furnace vacuum system was closed off and exposed to a 10 sccm H_2, 10 m Torr environment while the temperature was raised 950 °C. The quartz tube was held at this temperature for 30 min to remove any generate oxide layer on the Cu. The process involves passing Hydrogen flow and carbon source (Methane) vapor (typically 60 min) through the quartz tube in which a copper foil's material is placed at a sufficiently high temperature 950°C under high vacuum (10^{-4} torr) to decompose the hydrocarbon to form graphene sheet. After growth graphene sheet, a stream of pure ferrocene powder has sent inside the tubular reactors leading to the formation of the first nuclei believe slowly on graphene sheets on top of cupper foils, as shown in Figure 3.1. Volatile materials ferrocence directly turn from solid to vapor, and perform CVD while passing over the substrate kept in the high-temperature zone. Subsequently, the furnace heating system was rapidly cooled to room temperature. In addition to the condition for the fabrication magnetic NPs at 950°C, other specimens were fabricated to investigate time effect on iron carbide NPs the conditions.

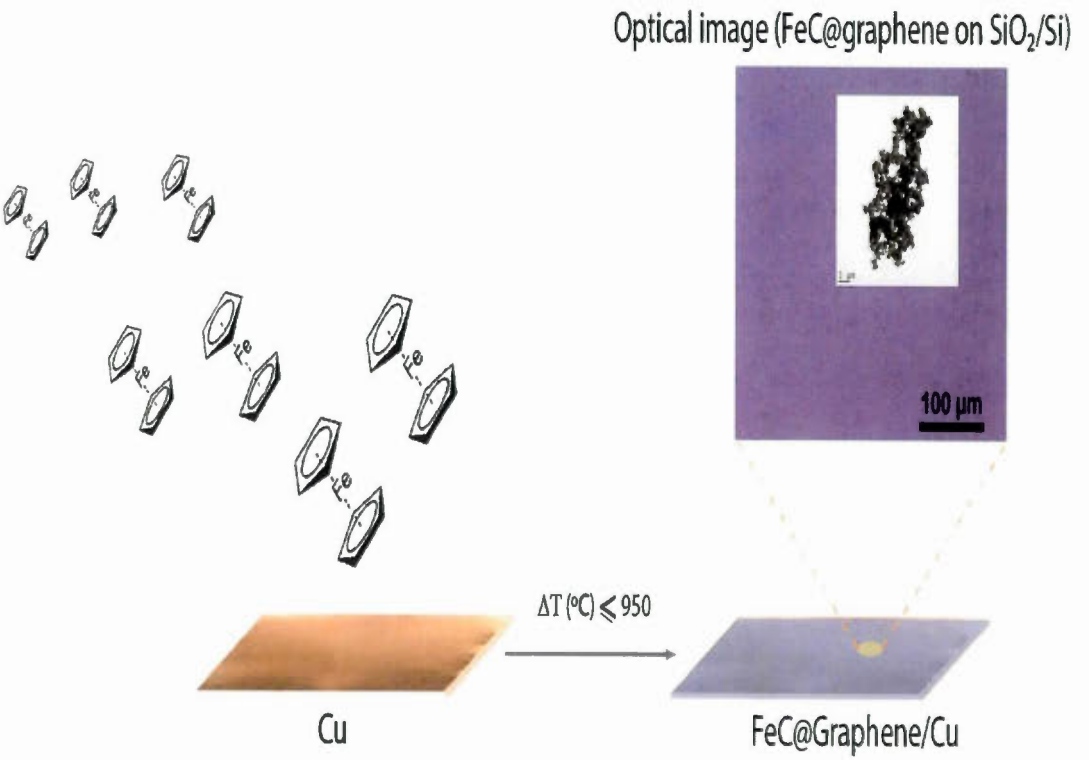

Figure 3. 1 FeC@Graphene on top of graphene covered Cu (M.Alahmadi, 2016)

3.1.1 FeC@Graphene nanoparticles growth

A one-step in-situ route to free standing core-shell iron carbide nanoparticles on monolayer graphene is presented. The core-shell FeC@Graphene nanoparticles growth was realized by a simple chemical vapor deposition process, where ferrocene precursors are introduced into the growth chamber. The simultaneous growth of graphene and iron carbide nanoparticles enables uniform nanoparticle formation.

The SEM image of FeC@Graphene nanoparticles synthesized by CVD method was shown in Figure 3.2. SEM showed the formation of silver nanoparticles with an average size of 50-80 nm. It gave a clear image of highly dense FeC@Graphene nanoparticles. However, to investigate the particle density distribution, a kinetic study was carried in which different growing exposure times at constant introduction flux of ferrocene precursors are used. In order to investigate the effect of ferrocene time introduction to the CVD chamber on the dispersion of the FeC@Graphene NPs, we present our results on samples grown at different exposure time at constant introduction flux of ferrocene precursors, namely, from 1h to 7h as shown in Figure 3.2 growth. The particles are generally interconnected in these cases. This implies that coalescence prevents island formation and instead, a semi-continuous film is formed. We found that the exposure time is an important parameter that increases the FeC@Graphene NPs concentration. Therefore, at high exposure time typically between 6 to 7 hours, the FeC@Graphene NPs powder is formed in Figure 3.2. With increasing to exposure time FeC NPs, causing the formation of a greater number of NPs as well as increasing the graphene layers of shell. The ability to separate and controlled placement of magnetic FeC@Graphene NPs by means of an external magnetic field, as shown in Figure 3.3. Therefore, the FeC@Graphene NPs can be regarded as excellent potential magnetic probes for various biological applications in which both manipulation and monitoring are required.

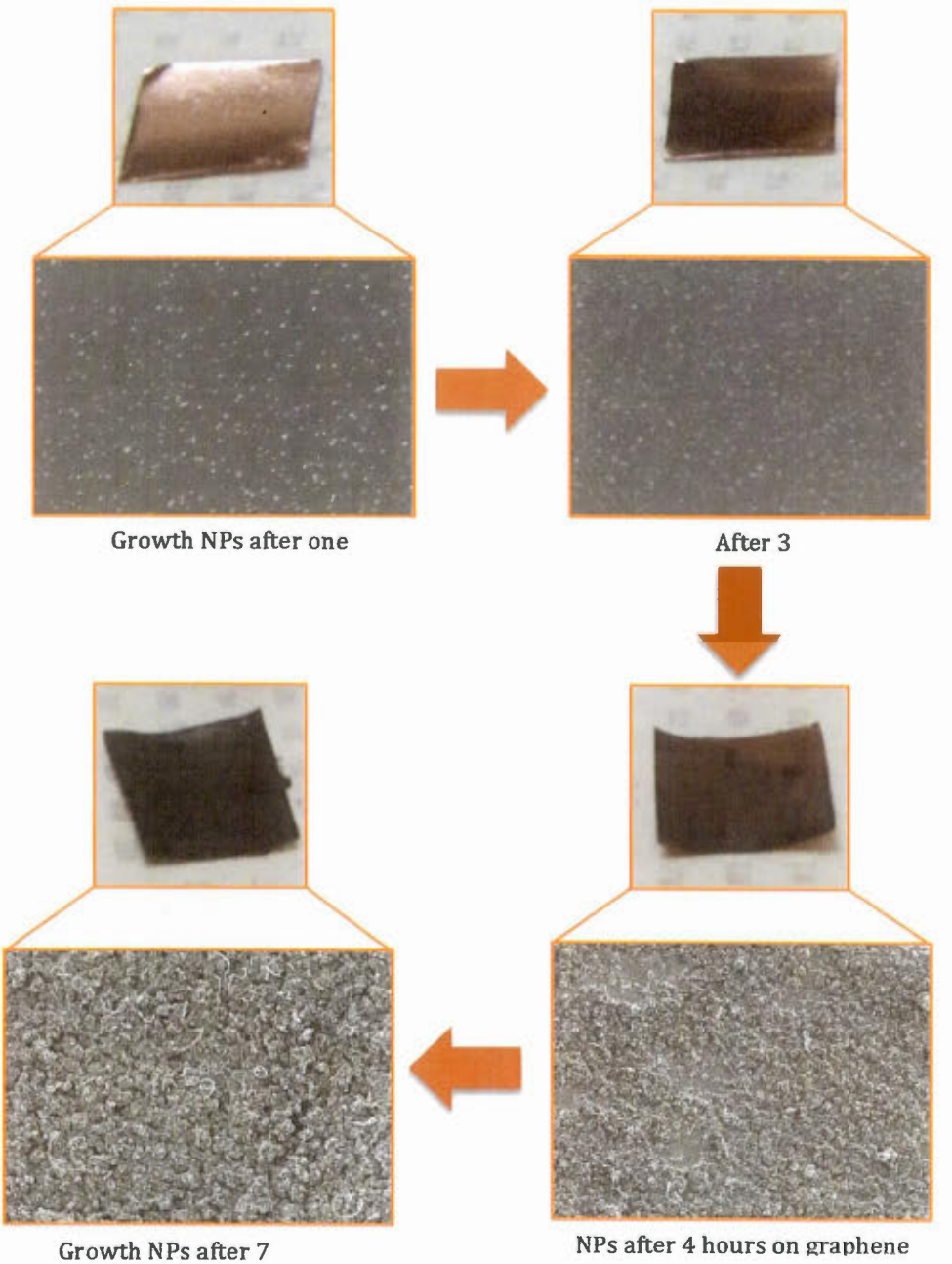

Figure 3. 2 Increase deposition of FeC nanoparticles on the top of graphene with increasing exposure time from1 hour to 7 hours (M.Alahmadi, 2016)

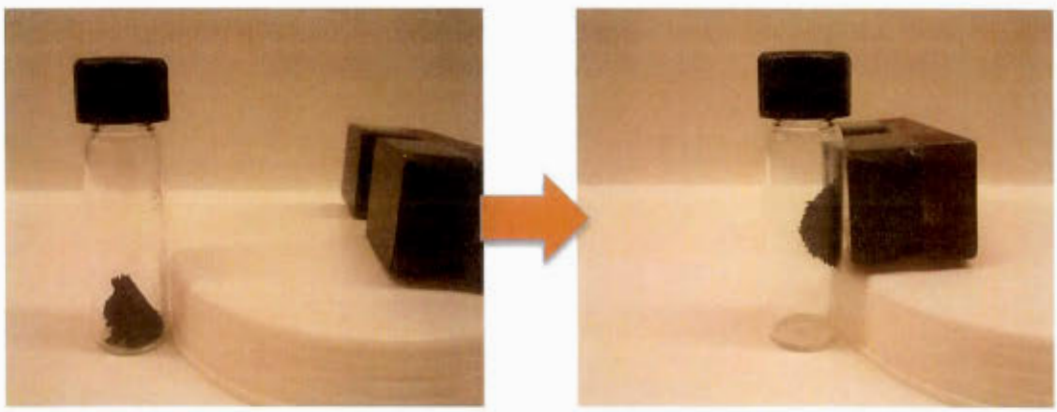

Figure 3.3 Photographs of FeC@Graphene NPs powder without (a) and with magnet (b)

3.2 Transmission Electron Microscopy observation (TEM)

Morphological and structural details of as-obtained FeC@Graphene nanoparticles were investigated by the quantity of black spherical mass are present (Luo et al., 2010). Figure 3.4a demonstrates a typical TEM (transmission electron microscopy) image of the product, indicating that the product mainly consists of well-dispersed iron carbide nanoparticles with size ranging from 60 to 80 nm, which are encapsulated in carbon matrix and also found that a spherical particle was located in the center of the product particle (Fan, Ma, Ju, & Li, 2008). Figure 3.4b shows a typical higher-magnification image of the single nanoparticle as marked by a circle in Figure 3.4a. It clearly indicates that the spherical nanoparticle has core–shell

morphology and several graphitic layers closely encapsulated these nanoparticles. Figure 3.4c is a circle partial magnification image of the particle in Figure 3.4b. Further, lattice fringes can be seen clearly for both the core and the shell in Figure 4.4c, suggesting that both the core and the shell are crystalline. Figure 3.4d selected area electron diffraction (SAED) analysis shows that the main state of the iron-containing nanoparticles was determined to be ca. 0.185 nm, which agrees with the d (lattice plane distance) of the orthorhombic iron carbide crystal. In the SAED pattern of the carbon structure (3d), five clear diffraction rings (1.70°), (1.04°), (0.61°), (0.54°) and (0.85°) are observed showing good graphitization of iron nanoparticles and the interlayer distance between shells is about 3.4 A°, which is typical matches the interlayer spacing value (3.354 A°) of graphite (Fan et al., 2008) (Lian et al., 2008).

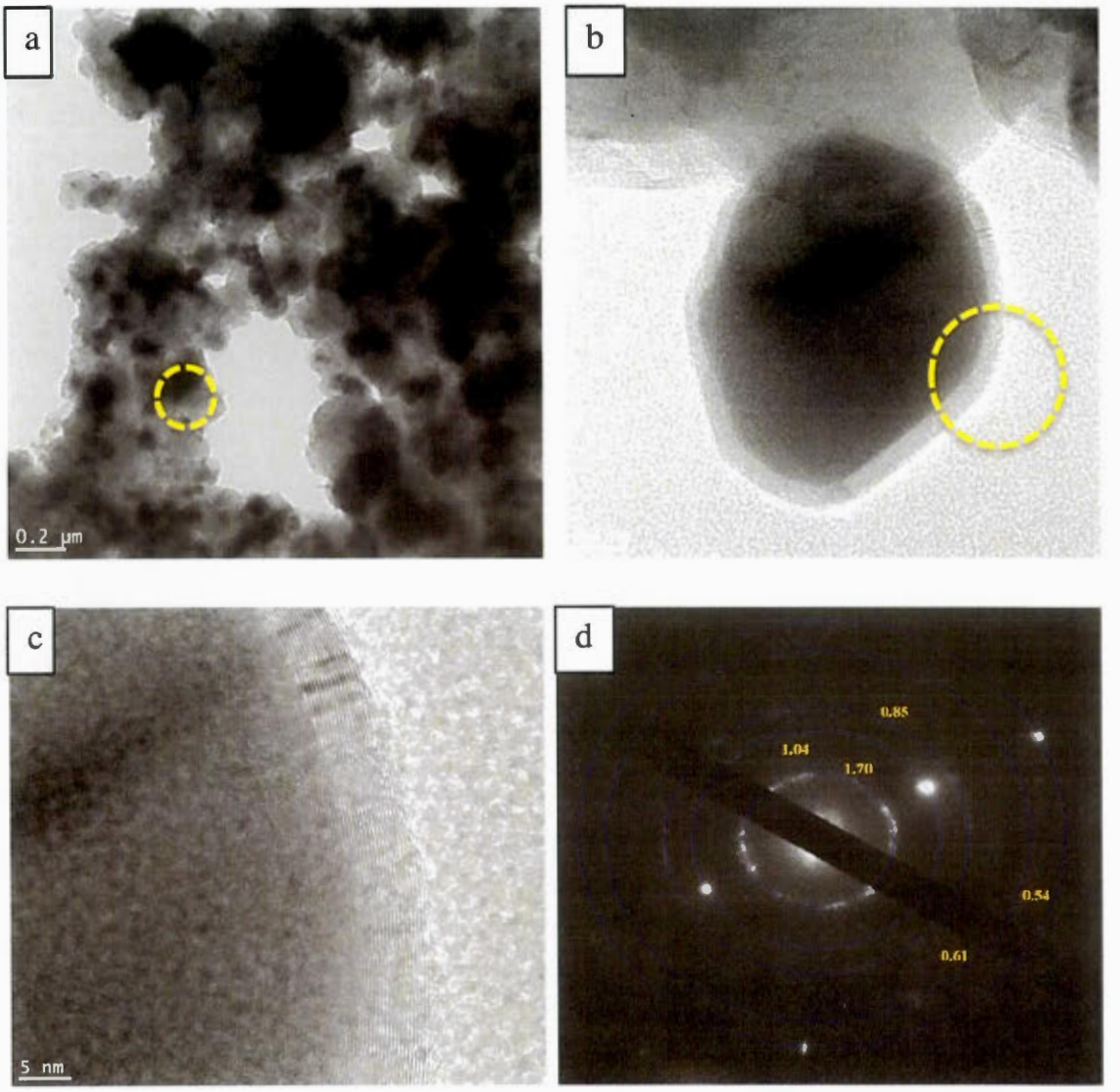

Figure 3. 4 TEM images of the carbon-encapsulated iron carbide nanoparticles from product. (a) TEM image of FeC@Graphene nanoparticles in the carbon matrix at low magnification. (b) HR-TEM image of a typical single graphene/Fe shell/core nanoparticles about 60–80 nm .The insert shows lattice fringes of FeC@Graphene. (C) Higher- partial magnification of the region marked in the image (b). A typical selective area electron diffraction (SAED) of product (M.Alahmadi, 2016).

3.3 XRD Pattern Analysis and EDS

XRD spectra were acquired between 2θ angles of 5-2.50°, with a step size of 0.02° and step time 0.6s. Figure 3.5a presents diffraction patterns of FeC@Graphene NPs product. Tow diffraction peaks located at 52.5°, and 77.2° can be attributed to the tow crystalline planes of the face centered cubic iron. The peaks at 30.8°, 54.5°, 75.9°, 64° and 69.5° can be attributed to the diffraction of carbon. In order to further confirm the chemical compositions of these graphene/Fe shell/core nanoparticles, elemental composition microanalysis was performed by EDS. Figure 3.5b exhibits a typical EDS spectrum of the sample synthesized at 950°C, whose peaks are assigned to C and Fe, no other element has been detected in the synthesized products. The copper peaks arise due to the copper grid supporting the TEM-specimen.

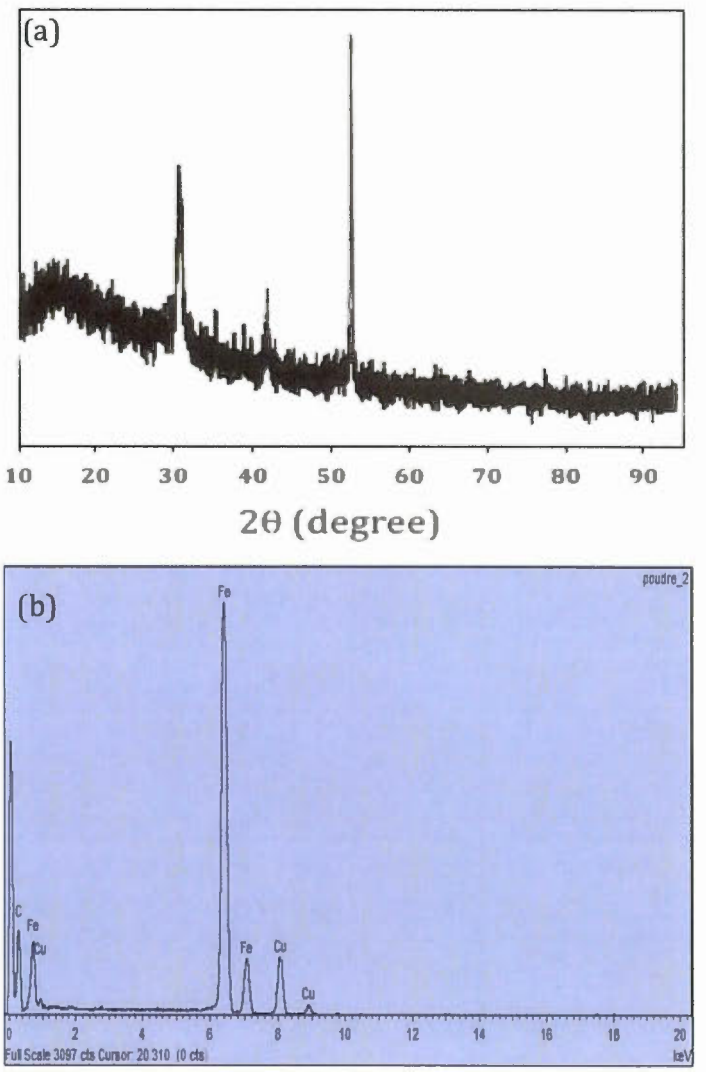

Figure 3. 5 (a) The X-ray diffraction pattern of iron carbide nanoparticles product. (b) EDS spectrum obtained from a FeC@Graphene nanoparticle (M.Alahmadi, 2016)

3.4 Raman Spectroscopy

Raman spectroscopy allows characterization of many types of samples without any specific preparation. The Raman spectra were obtained using the 514 nm laser line for excitation equipped with a microscope and CCD detector. Raman measurements were performed at room temperature and atmospheric pressure. As shown in Figure 3.6, the characteristic peak positions of iron nanoparticles were determined in the zoom region where major features of the wavenumber are observed at about 221.58, 287.72, 407.62, 495.91, and 608.67 cm^{-1} for the iron stretching vibration (Madhavi, Prasad, & Madhavi, 2013). Also; from this region the absorption peak intensity of iron in sample three increases with the increasing of NPs in the top of graphene layers. Furthermore; the spectrum indicates that presence mode characteristics of graphene NPs for D and G bands. The D-band at ~1350 cm^{-1} is known as the disorder band. The band is typically very weak in graphite and is typically weak in graphene as well. D-band indicates that there are a lot of defects in the material. The intensity of the D-band is directly proportional to the level of defects in the sample. The G-band at about 1580 cm^{-1} is the primary mode in graphene. It represents the planar configuration sp^2 bonded carbon that constitutes graphene. It is extremely sensitive to strain effects and is also a good indicator of the number of graphene layers. As the number of layers increases, the G band position shifts to lower frequencies. The 2D-band is the second order of the D-band, sometimes referred to as an overtone of the D-band. This feature appears at approximately 2700 cm^{-1} for a 514 nm laser

excitation and can also be used for the determination of the number of graphene layers. As the amount of disorder in graphene increases, the Raman intensity increases for the three separate disorder peaks: D (1350 cm^{-1}, D´ (1620 cm^{-1}), and D+G (2940 cm^{-1}) (Hodkiewicz, 2010) (Lancelot, Lille, & Ascq, n.d.).

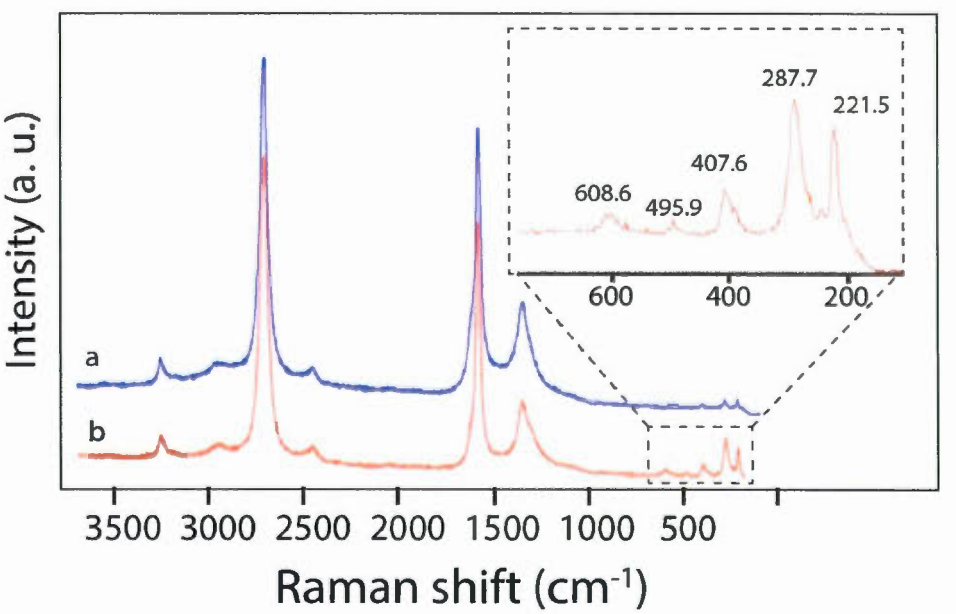

Figure 3. 6 Raman spectra for FeC@Graphene NPs obtained according to the synthesis time by using a 514 nm excitation laser, and the absorption peaks in zoom region between 200 and 800 cm^{-1} increase with the increasing NPs at the top of graphene layers (M.Alahmadi, 2016).

3.5 Magnetism analysis

The magnetic properties of the nanomaterials have been believed to be dependent on the nanoparticle shape, crystallinity, magnetic composition and so on. As the particle size became smaller in diameter of 10–100 nm, such a surface effect was more evident (Luo et al., 2010). The hysteresis loop (Figure 3.7) of the encapsulated particles measured at 290 K temperature intrinsic magnetic properties with remnant magnetization, saturation magnetization, and the ratio of remanence to saturation, and coercivity values, respectively, shown in Table 2.

The observed M–H loop in Figure 3.7 indicates the product has a coercive force of 0.022 Oe, which are close to the characteristics of superparamagnetism response. We recognized that the saturated magnetization value (M_S) was 42.5 emu/g and the remanence magnetization value (M_r) was 4.03 emu/g. It is clearly seen that the ratio of remanence to saturation (M_r/M_S) was 0.095. The shape of the hysteresis curve suggests that there is a mixture of ferromagnetic and superparamagnetic nanoparticles particles.

Table 2: Comparison of saturation magnetization (M_S) remnant magnetization (M_R) coercive field (H_c), ratio M_R/M_S for core-shell FeC@Graphene nanoparticles				
Product	**M_R (emu/g)**	**M_S (emu/g)**	**M_R/M_S**	**H_C (Oe)**
FeC	4.03	42.5	0.095	0.022

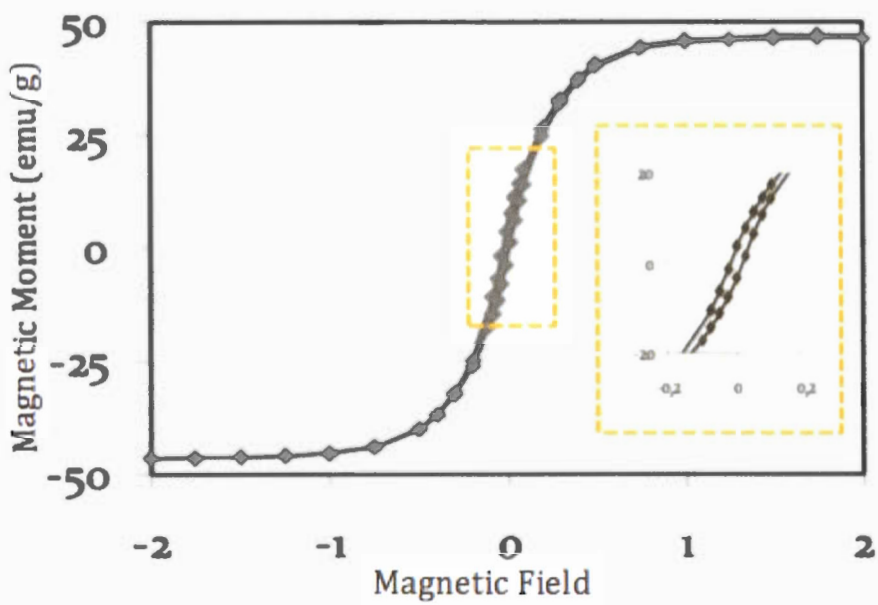

Figure 3. 7 Magnetic hysteresis loops measured for core-shell FeC@Graphene synthesized by CVD at 290 K (M.Alahmadi, 2016).

3.6 Conclusion

In this work, we have successfully developed a low-cost, high-yield and one-step metal-organic CVD FeC nanoparticles on top of graphene multilayer at 950°C. The results showed that the average particle size of the FeC@Graphene NPs were approximately 60 nm. Furthermore, we found that the FeC nanoparticle was dependent on exposure time. The major difference between FeC NPs according to exposure time is the sizes diameter of core nanoparticles, which is roughly five times greater with increasing time from 1 to 7 h. We also found that synthesis nanoparticles at 7 hours, at much high concentrations result in a more significant increase of the size nanoparticles. Iron carbide nanoparticles have been characterized by the techniques of TEM, XRD, HR-XPS, and Raman. Moreover, the nanoparticles remained magnetic after coating with multi-layer graphene sheet.

CHAPTER IV

FUNCTIONALIZATION AND CHARACTERISATION OF FEC NPS SURFACES

4.1 INTRODUCTION

The work in chapter III exhibited the synthesis and characterization of magnetic FeC@Graphene NPs. The scope of this chapter describes different functionalizations, which have done on the surface of magnetic NPs, used during this thesis. For Characterization methods, studying the most common characterization techniques that use to investigate the modified magnetic FeC NPs.

Functionalization of the NPs can be defined as the addition of a chemical functional group on their surface in order to achieve surface modification that enables their self-organization and renders them compatible. NPs have mainly been functionalized with thiols, disulfides, amines, nitriles, carboxylic acids, phosphines and biomolecules. The diazonium chemistry is one of the most commonly adopted approaches to functionalize graphene surface. The covalent bonding of the aryl groups onto the graphene basal plane transforms the sp^2 carbon atoms into the sp^3 hybridization state, while the backbone framework of graphene is preserved (Zhu et al., 2012). The

spontaneous chemical functionalization of diazonium salt is one of the famous reactions to chemically dope graphitic carbon structures. The chemical functionalization of diazonium salt molecules has been first demonstrated to modify HOPG and glassy carbon surfaces by electrochemical reduction, which is known as the Saevant method. This is the first example of covalent bond formation of diazonium salts molecules to graphitic carbons without preoxidation process. Similar reactions have been attempted on carbon nanotubes and graphene as well. Several research groups including Smalley and Shim groups have reported that metallic carbon nanotubes can be selectively and covalently functionalized with diazonium salts even without external energy source (Lim, Lee, Shin, Shin, & Choi, 2010). The surface chemistry of graphene is expected to be similar to that of graphite and related carbonaceous materials such as carbon nanotubes. One of the most versatile and facile methods of covalently grafting organic molecules onto these carbonaceous materials is the reduction of aryl diazonium salts ($Ar\text{-}N{=}N^{+}X^{-}$) through either electrochemical or spontaneous reduction with the substrate. In this reduction process, the aryl diazonium cation accepts an electron from the substrate and generates an aryl radical by releasing a nitrogen molecule. The highly reactive aryl radical can then covalently react with graphitic substrates and possibly with other surface mounted aryls leading to aryl oligomers (Hossain, Walsh, & Hersam, 2010) (Murphy, Cullen, Jayasundara, Scanlan, & Colavita, 2012) as shown in Figure 4.1.

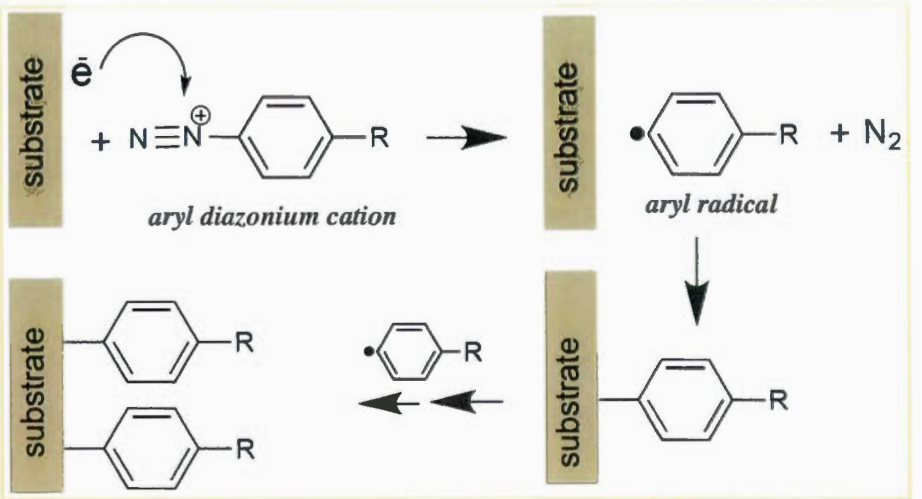

Figure 4. 1 Mechanism for the Aryl Groups bonding onto surface .The aryl diazonium cation accepts one electron from the substrate and forms an aryl radical through the release of a dinitrogen molecule. The aryl radical can then covalently react with the surface or with other surface mounted aryls leading to aryl oligomers. Modified form (Hossain et al., 2010).

4.2. Results

4.2.1 Functionalization

4.2.1.1 Chemical functionalization of FeC NPs with P-nitrobenzene diazonium Salt

Herein a convenient method to obtain chemical modification by covalent attachment with *P*-nitro phenyl groups onto magnetic FeC@Graphene NPs. The surface modification was achieved through the spontaneous reaction of the diazonium salt with the graphene layer as illustrated in Figure 4.2.The reaction is due to spontaneous electrons transfer from the graphene layer and its substrate to the diazonium salt. In

particular, the grafting was observed by X-ray photoelectron spectroscopy and IR infrared spectroscopy (in the following chapter) with iron NPs as the substrates.

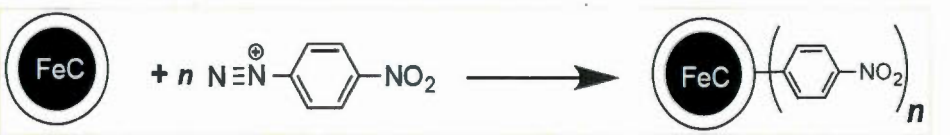

Figure 4. 2 Schematic illustration the spontaneous grafting of aryl groups to surface of NPs via reduction of 4-nitro phenyl diazonium (NPD) tetrafluoroborate.

4.2.1.2 Amino-functionalized FeC NPs by Chemical nitro reduction

The preparation of amino-functionalized FeC@Graphene involves reducing aromatic *P*-nitro phenyl groups to the corresponding anilines by chemical nitro reduction. The amino-termination allows further chemistry of the function-nalized NPs and makes possible covalent bonding to polymers and biological systems such as protein, DNA and carbohydrates. The chemical versatility of the amino group will allow controlled covalent bonding to polymers or biological molecules. The reaction schemes are shown in Figure 4.3.

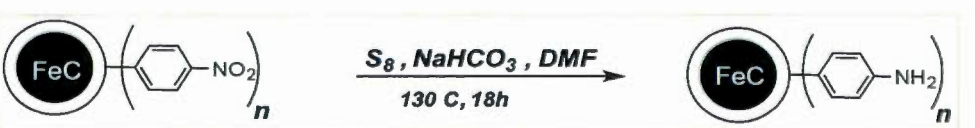

Figure 4. 3 Schematic of the chemical nitro reduction to form FeC NPs with amino functionalization group

4.2.1.3 Activated amino group

The following functionalization is to activate P-aminophenyl FeC@Graphene NPs by using glutaraldehyde linker as biofunctional cross linker agent, followed by coupling of antibodies β-lactoglobulin. Cross-linking glutaraldehyde reagents may be used to activate groups that exhibit low reactivity in an aqueous environment (e.g. carbodiimide for binding to COOH groups), or to join groups that are simply not reactive toward one another (e.g. NH_2). Also, the presence of glutaraldehyde may be useful in the creation of additional covalent bonds between the antibodies β-lactoglobulin and the nanoparticles. Typically, activation of amines groups in the magnetic NPs by glutaraldehyde and then coupling to the β-lactoglobulin provides good coupling (Eissa, Tlili, L'Hocine, & Zourob, 2012). The presence free amino groups (NH_2) which placed outwards the magnetic FeC@Graphene NPs was further activated by glutaraldehyde as a biofunctional cross linker .The reaction scheme is shown in Figure4.4. Typically, the aldehydes on both ends of glutaraldehyde will couple with free amines group of (NH_2)-FeC@Graphene to form a Schiff-base linkage and provides a free terminal aldehyde group with highly efficient at protein conjugation which can be condensed with free amino groups in antibody β-lactoglobulin molecules to form a second Schiff-base. The results indicated that the activated 4-aminophenyl FeC@Graphene NPs surface by glutaraldehyde was effective for immobilization of the antibodies β-lactoglobulin (Ibrahim, Al-Salamah,

El-Toni, El-Tayeb, & Elbadawi, 2013) (Petkova, Záruba, Žvátora, & Král, 2012) (Rocha, Gil, & Garcia, 1998).

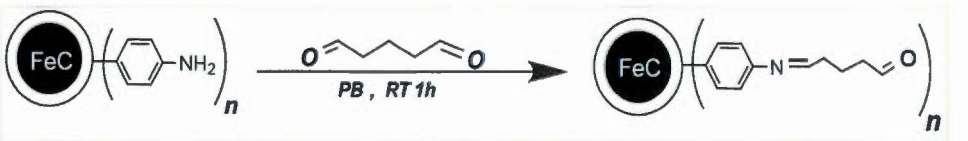

Figure 4. 4 Activation of amino group after chemical nitro reduction by using glutaraldehyde linker

4.2.1.4 Conjugation of β-lactoglobulin Antibodies with Glutaraldehyde

The following functionalization is to immobilize Affinity-purified antibodies β-lactoglobulin onto FeC@Graphene surface. Immobilizations were carried out at 25 °C via cross linker glutaraldehyde coupling. Figure 4.5 a typical antibody β-LG immobilization procedure involves activation NPs surface with glutaraldehyde linkers, followed by β-lactoglobulin antibodies.

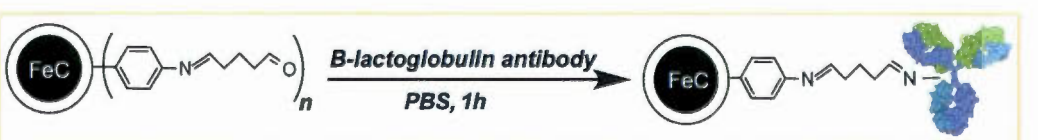

Figure 4. 5 Activation amino groups by using glutaraldehyde and covalent immobilization of proteins

4.2.2 Morphological and structural characteristics of the graphene/iron shell/core nanoparticles

4.2.2.1 X-ray Photoelectron Spectroscopy

X-ray photoelectron spectroscopy (XPS) was further used to evaluate the chemical composition of the modified FeC@Graphene NPs surfaces and to follow the changes of the chemical bonding associated with transformations occurring on the surface (Actis et al., 2008). Figure 4.6A displays the high-resolution XPS C1s spectrum of NPs with four components. After the chemical modified NPs, the single peak at 284.2 eV, which is due to the sp^2 hybridized C atoms and the binding energy at 285.3 is due to sp^3 carbon. The most importance peaks are at a binding energy of 285.57 eV (assigned to C-N) while the peaks at 287.5 eV correspond to carbons of the C=O functional groups (Bekyarova et al., 2009) (Davydov et al., 2014).

There are two peaks in the N1s XPS spectrum of FeC@Graphene NPs (see Figure 6.4B). The distinct sharp peak at higher binding energy 406 corresponds to the nitrogen in the nitro group. The broad peak at 399 eV is attributed to nitrogen in the lower oxidation states. This peak was observed earlier in the study of epitaxial graphene grafted with 4-nitro phenyl groups and was explained by reduction of the nitro groups by X-ray radiation in the XPS spectrometer chamber. A plausible alternative process could be *in situ* electrolytic reduction of the nitro groups by electrons from neighboring islands of intact graphene. Alternatively, the 399 eV peak could correspond to diazenyl groups introduced by electrophilic attack of the

diazonium cation on aromatic rings (azo coupling reaction)(Kosynkin, Bockman, & Kochi, 1997) (Bekyarova et al., 2009). In the same figure the second peak in the bottom trace show the amine functionalization FeC@Graphene NPs at binding energy 399 eV. In addition, the absence of a peak around 400 eV (see Figure 4.6B) confirms the reduction of the nitro group as it is converted to an amine.

Figure 4.6C displays the O1s XPS spectra of functionalization NPs. O1s XPS spectrum that was obtained from the coated iron nanoparticles illustrates that no significant peak was obtained in the spectrum as FeC@Graphene NPs produced, (in the bottom spectra). The centric single peak is appeared at 530 eV referred to chemical nitro grafting of P-nitro phenyl bound to the surface of NPs (in the second bottom spectra). The peak due chemical reduction of nitro groups disappears in this figure (in second spectra from the top), suggesting that the nitro group in aromatic nitro compounds reduced at 130°C temperature to corresponding amine groups. For the survey of Fe2p core levels Figure 4.6D, the photoelectron peaks at 710.56 eV, 719.26 eV and 723.91 eV represent the binding energies of Fe ($2p_{3/2}$), shake up satellite $2p_{3/2}$ and $2p_{1/2}$, respectively (Sun, Li, Cao, Zhang, & Wang, 2006).

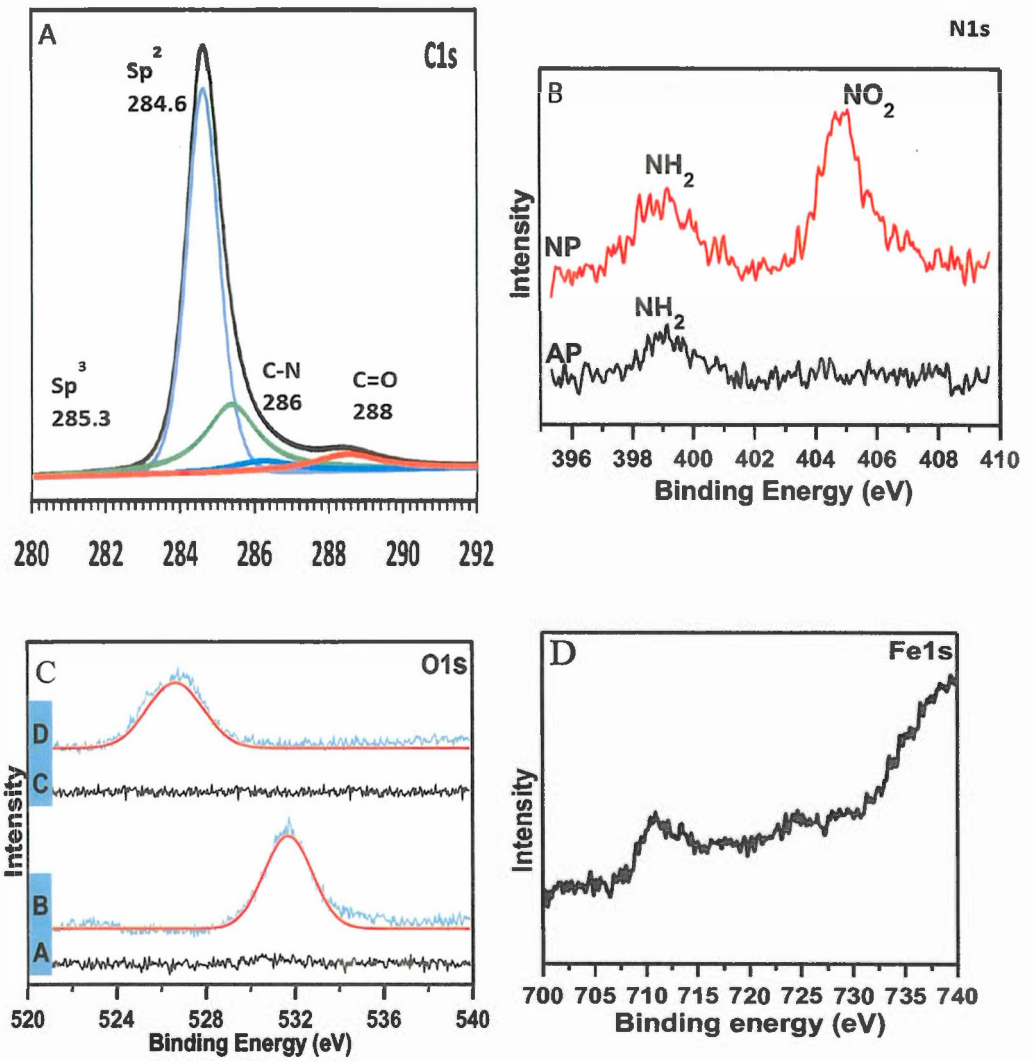

Figure 4. 6 Display High-resolution XPS for product (A) XPS C1s spectra after the chemical modification of NPs with GA (B) N1s spectra after the functionalization NPs with nitro phenyl (top row) and aminophenyl (bottom row) (C) O1s XPS spectra (a) before functionalization (b) modified with NP (c) after reduction nitro group (d) modified NPs with GA (D) High-resolution XPS Fe_2P.

4.2.2.3 Infrared Spectroscopy

The qualitative analysis of the various chemical functional groups ware performed by FT-IR. Figure 4.7 FT-IR spectra present modified core-shell graphene NPs. In the top spectrum displays FeC@Graphene NPs before functionalization process. In second trace from the top, the spectrum of the nitro phenyl functionalized iron carbide nanoparticles exhibit new bands at 1565 and 1378 cm^{-1}, which fall within the range of the symmetric and asymmetric stretching modes of the NO_2 group (Bekyarova et al., 2009). In second trace from the bottom, it displays the modification core-shell NPs with attached amino groups. The peaks due to amine group have been attributed to N–H stretching at 3300 cm^{-1}. The scissoring in-plane bending mode of the primary amine NH_2 group at 1645 cm^{-1} is broader than other peaks in this region while aliphatic C–N stretching at 1020-1220 cm^{-1}. The presence and location of the NH_2 and C-N bands confirm the presence of the saturated primary amine (Ramanathan, Fisher, Ruoff, & Brinson, 2005).The next step was based on the reaction between aminogropes and cross-linker glutaraldehyde (GA), which was used to cross-link the amino groups with antibodies due to the formation of an imine. Herein, the amino groups were changed to aldehyde groups. The amine groups–GA linking is shown in bottom trace , in which the bands due to the formation of imines in the area between 1900 and 1600 cm^{-1}, and the bands related to the stretching of C–N, C–C groups in the range 1500–1200 cm^{-1} are visible (Mura et al., 2012).

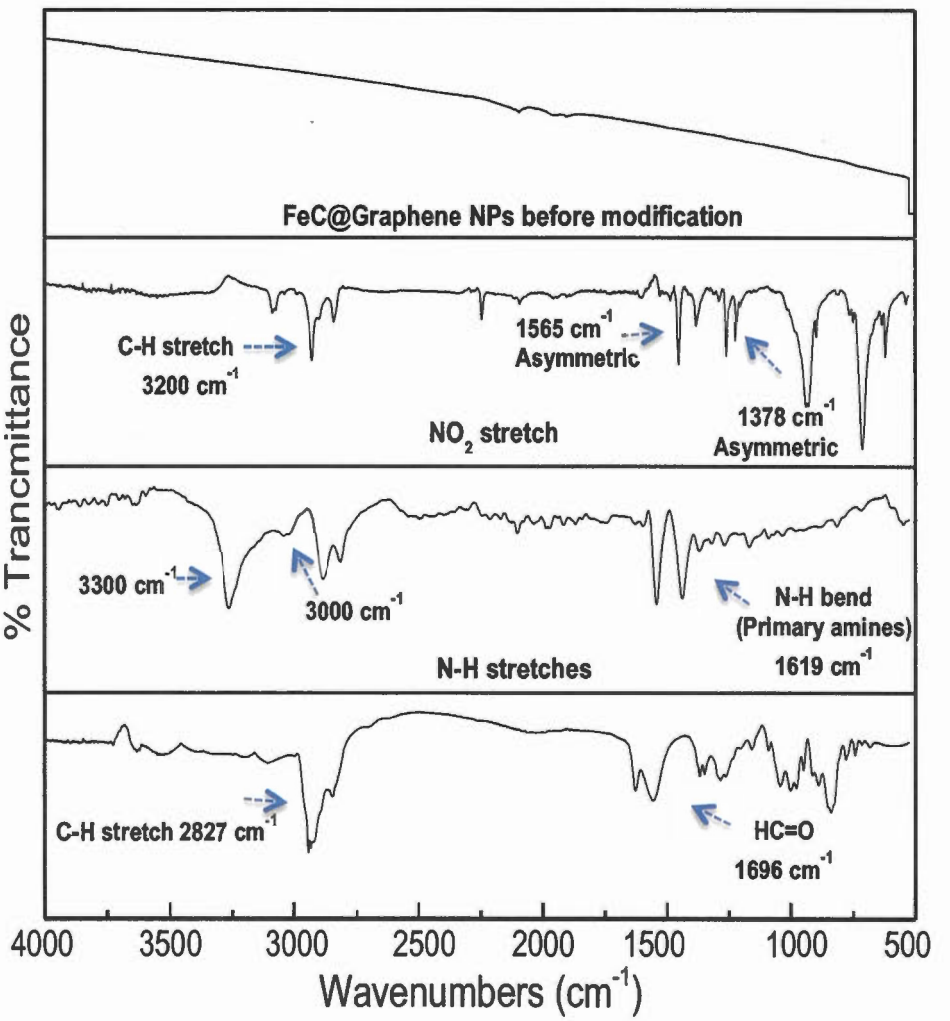

Figure 4. 7 IR spectra of the unreacted FeC@Graphen NPs powder (top trace), after a reaction with 4-nitro-benzenediazonium salt (second trace from the top), subsequent reduction with $S_8/NaHCO_3$ (second trace from the bottom) and glutaraldehyde linker (bottom trace)

4.3 Conclusion

The principal concept in this chapter is to bind biomolecules (β-lactoglubulin antibody) into iron carbide NPs surface by means of using functionalization layer. Herein introducing different covalent functionalization methods for graphene-coated iron carbide NPs were developed. In the first place, nitro groups were introduced to the surface of iron nanoparticles by spontaneous reaction with P-nitrobenzenediazonium tetrafluoroborate (*P*-NBDT) to from 4-nitrobenzen. In the second place, aminophenyl functionalized magnetite nanoparticles were successfully synthesized by chemical nitro reduction chemistry of nitro groups and were activated by using glutaraldehyde linker and used for the covalent bonding with antibodies. Finally, Anti-β-lactoglubulin, which has amine terminal groups, successfully immobilized by covalent attachment to these activated magnetic nanoparticles by using glutaraldehyde as linker. Moreover; after FeC@Graphene NPs were functionalized, X-ray Photoelectron Spectroscopy (XPS), scanning electron microscopy (SEM), Raman spectroscopy, transmission electron microscopy (TEM), and hysteresis loops were conducted to characterize the morphological, chemical, structural and magnetic properties of graphene/Fe shell/core nanoparticles. The resulting functionalized graphene-coated iron carbide NPs allows a significant immobilization of β-lactoglubulin, and improving the sensitivity of the immunosensor.

CHAPTER V

ELECTROCHEMICAL IMMUNOSENSOR BASED ON MODIFIED NPS

The work presented in chapter IV yielded functionalization core-shell iron carbide graphene nanoparticles .The objective of the current chapter is using modified core-shell FeC@Graphene nanoparticles to develop a fast, simple, lower cost, and sensitive detection method for β-Lactoglobulin (β-LG) based on using electrochemical immunosensor. Also, herein we show the fabrication process of immunosensor. This technique can detect low concentration of β-LG. Also, using external magnetic field to control modified nanoparticles on carbon screen-printed electrodes enhanced the electrochemical immunosensor.

5.1 Concept of Biosensors

The biosensors are devices that register a biological change or reaction, which is converted into a signal that can be detected and quantified. A typical biosensor contains bioreceptor, which has biological recognition molecules with highly selective and specific to the target analyte(s) and transducer can be carried out by different means, taking advantage of different properties changes or signal

generation, which occurs following the formation of antigen-antibody complex (see Figure 5.1)(Ronkainen & Okon, 2014). The bioreceptor molecules of an immunosensor are the antibodies. The antibodies are also called immunoglobulins, because they are proteins related to the immunological system. The immunoglobulin G (IgG), the main antibody in the serum, consists of four polypeptides: two heavy chains and two light ones, joined to form a "Y" shaped molecule. The amino acid sequence in the tips of the "Y" varies greatly among different antibodies. This variable region, composed of 110-130 amino acids, give the antibody its specificity for binding the antigen. The variable region includes the ends of the light and heavy chains. Each antibody has a unique structure that attaches to an antigen in a lock-and-key fit. When the antibody is attached to the antigen, the antigen is destroyed or marked for destruction or elimination by some other method. The constant region determines the mechanism used to destroy antigen. The antibodies are divided in five main classes, IgM, IgG, IgA, IgD and IgE, according to the structure of the constant area and its immune function (Ramírez, Salgado, & Valdman, 2009).

Transducer or the detector device that is in contact with the electrochemically active interface, usually an electrode, converts that biochemical formation of antigen-antibody complex reactions into an electrical signal that may be amplified further by a signal processor and registered as an analytical result. The signal processor includes computer software that converts the electrical signal into a form that may be displayed onto a computer screen (Ronkainen & Okon, 2014). Although; there are many kinds of transducers include; optical, thermal, magnetic, and acoustic, this

chapter is concerned with biosensors where the transducing mechanisms are related to the measurement of electrons. Therefore, the transducers employed in immunosensors can be summarized as follows: Electrochemical transducers. In this case, an electrical signal is measured, which shows significant differences in magnitude if antigen-antibody complex are formed. The main electrochemical transducers are amperometric (measuring of current) which we used in this work, potentiometric (measuring of electrode potential or voltage differences) and conductimetric (measuring of conductivity or resistance) (Moina & Ybarra, 2012).

5.2 Antibodies β–Lactoglobulin

β-Lactoglobulin (β-LG), the major protein of bovine whey, is a 162-amino acid containing globular protein with a molar mass (Mw) of 18362 g/mol, and well established primary, secondary, tertiary, and quaternary structures Figure 5.2 (Croguennec, Mollé, & Mehra, 2004). β-Lactoglobulin is the major whey protein in the milk of ruminants, horses, pigs, cats, dogs, dolphins, whales, and kangaroos but not in the milk of humans, rodents, and lagomorphs (Patel, Chauhan, Singh, & Soni, 2007).Although β-LG is considered to be available protein in view of nutritional science, β-LG is a potent allergen of milk allergies; ~82% of milk allergy patients are sensitive to β-LG (Aoki, Iskandar, Yoshida, Takahashi, & Hattori, 2006) (*Spies, J. 1973 . J. Milk Food Technol., 36: 225–231*, n.d.). Therefore, reliable detection methods are needed for regulatory agencies and the food industry to protect allergic consumers. Up to now, various analytical methods have been developed for the

detection of β-lactoglobulin such as enzyme-linked immunosorbent assays (ELISA), HPLC and CE methods with laser-induced fluorescence (LIF) detection, and enzymes linked immunoaffinity chromatography (ELIAC). However, a developed alternative method with lower cost, higher sensitivity, selectivity and faster response is still needed. Electrochemical biosensors have found wide applications in various biomedical and environmental fields in recent years because of their low cost, fast response, sensitivity. Therefore, the developed electrochemical immunosensor presented herein is expected to have a potential role in food safety and consumer protection (Eissa et al., 2012).

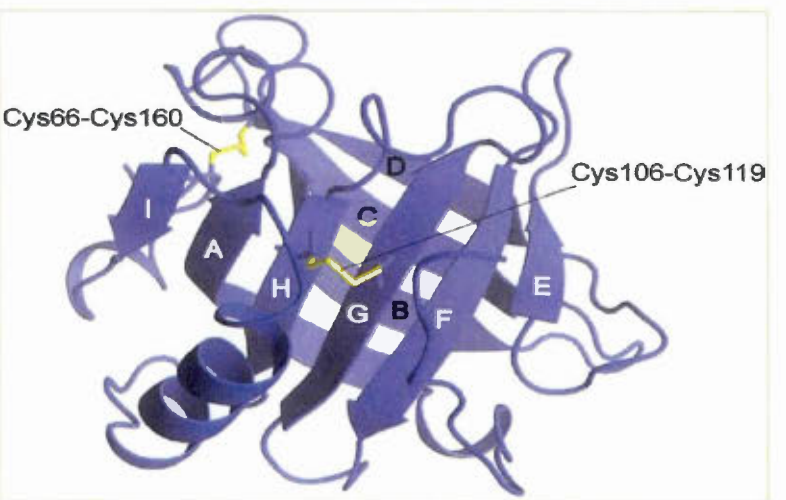

Figure 5. 1 Schematic representation of the three-dimensional structure of β–lactoglobulin (Ikeguchi, 2014)

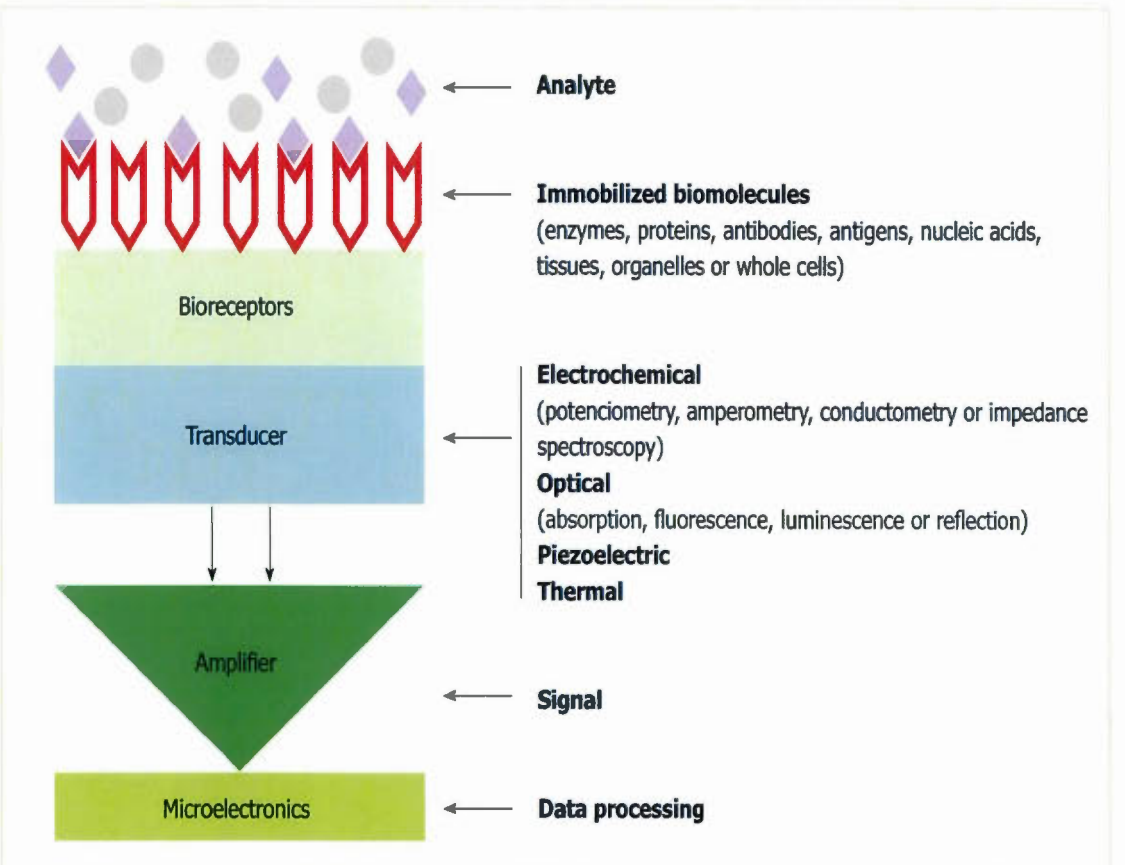

Figure 5. 2 Schematic structure and operating principle of a biosensor (Uliana, 2014)

5.3 Electrochemical Immunosensors

The fundamental basis of immunosensors is the specificity of the molecular recognition of antigens by antibodies to form a stable complex combined with solid-state devices, in which the immunochemical reaction is coupled to a transducer (Skládal et al., 2013) (Zhou et al., 2014). Immunosensors may be categorized based on the detection principle applied (e.g., electrochemical, optical, and microgravimetric immunosensors). Electrochemical immunosensors are concerned with the formation of a recognition complex between the sensing biomaterial and the analyte under investigation in a monolayer or thin-film configuration, on an electronic transducer (Tully, Higson, & O'Kennedy, 2008). Electrochemical immunosensors are used bio-recognition element linked with electrochemical transducers. This means that the biological recognition is measured by means of an electrochemical signal. Electrochemical detection methods, which are based on interfacial phenomenon, are better suited for detection in little sample volumes (from microliters to as low as nanoliters) as the sensitivity of these methods is independent of the sample volume used in the measurement. Extremely low detection limits may be achieved (zeptomols, 10^{-12} mol) with electrochemical detection. In these biosensors, the biological reaction is transformed into a measurable signal by the electroanalytical detection method. Additionally, most electroanalytical detection methods require little or no sample preparation prior to analysis. Also, the

electrochemical instruments that detect and record the signal tends to be inexpensive and are often portable, even handheld devices (Ronkainen & Okon, 2014).

5.3.1 Voltammetric Sensors

Voltammetry is perhaps the most widely used electrochemical method as it is also used for nonanalytical purposes by biochemists, materials scientists, chemical engineers, inorganic, and physical chemists. In addition to quantification of a redox active analyte, voltammetry can be used to: (i) monitor adsorption processes on surfaces; (ii) probe electron transfer mechanisms at electrode surfaces that have been chemically modified by nanoparticles or other materials; and (iii) perform fundamental studies of oxidation/reduction processes. Voltammetry is a broad term that describes all electroanalytical methods in which the applied potential is scanned over a set potential range at a steady scan rate (mV/s), while the resulting current is measured. Voltammetry is based on the measurement of current that develops in an electrochemical cell under conditions of complete concentration polarization. Voltammetric methods include linear sweep/scan voltammetry, cyclic voltammetry, hydrodynamic voltammetry, differential pulse voltammetry, square-wave voltammetry, ac voltammetry, polarography, and stripping voltammetry (Ronkainen & Okon, 2014).

5.3.2 Square-Wave Voltammetry (SWV)

Square-Wave Voltammetry (SWV) is a type of pulse polagrography that is fast and with high sensitivities. An entire voltammogram may be obtained in less than 10 ms by SWV. The extremely high sensitivity, which is key in immunosensor applications such as cancer biomarker detection, and the availability of commercial instruments capable of SWV have made this electroanalytical method more popular over the past few decades. The excitation signal in a potential *vs.* time plot may look like a "staircase" or a series of increasing pillars and troughs.

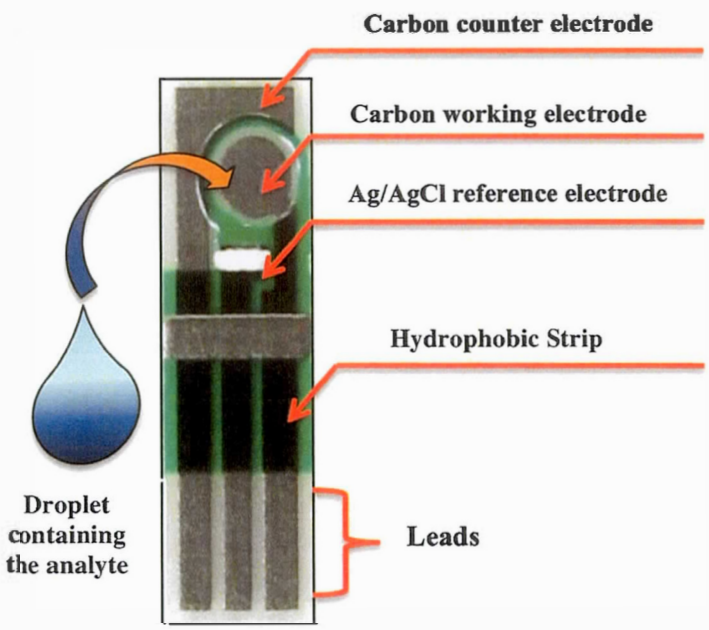

Figure 5. 3 Schematic of Carbon Screen-Printed Electrodes (SPEs) (M.Alahmadi, 2016)

5.4 Results

5.4.1 Instruments and techniques

The electrochemical experiment was carried out by using Auto-lab PGSTAT302N potentiostat/ galvanostat. A screen-printed carbon electrode (CSPEs) was purchased from Dropsens, Inc. (Spain, ref. 110GPH). Conventionally, the electrodes incorporate three-electrode configuration, which comprises a carbon-working electrode modified with FeC@Graphene NPs, carbon counter and Ag/AgCl electrode as reference electrode Figure 5.3.

5.4.2 Preparation of immunosensor

Phosphate buffers PB solution (200mM, pH 7.0, KH_2PO_4, K_2HPO4) was made from 0.8533 g Na_2HPO_4 and 0.847 g $KHPO_4$ in 250 ml nano-water, and the pH adjusted to about 7 using concentrated NaOH and was used to dilute the gluteraldehyde solution for the activation of the amine groups.

For the β-lactoglobulin measurements, required concentrations of antibodies β-lG were prepared in 10 mM PBS buffer pH 7.4, solution was pipetted onto the vials, which has magnetic FeC@Graphene nanoparticles and was incubated for 45 minutes. After the immobilization of β-lG antibodies on the magnetic nanoparticles antibodies

can be held onto vials. Obtained immunosensor was immersed into several concentration of β-lactoglobulin to complete an antigen-antibody interaction for 45 minutes. Then, the modified nanoparticles were washed with PBS solution and were extracted from vials by using a magnet filed to cover the working area of the screen-printed carbon electrodes (SPCEs) and dried in vacuo. The starting concentration of the lgG solution was 0.1 to 100 ng/mL. After every measurement, the electrodes were washed with PBS solution and water due to using the same electrode during the electrochemical measurement. Immunosensor are based on the interaction between the antibody and the antigen, gives high specificity and sensitivity to the immunoassay. All the electrochemical measurements were performed in 10 mM PBS (pH 7.0) containing 5.0 mM $[Fe\ (CN)_6]^{3-/4-}$ using Squarewave voltammetry (SWV) at room temperature. The decrease of the SWV current was relative to the concentration of β-lactoglobulin, which has been used to construct the calibration curve. The procedures used for construction of the immunosensor were shown in Figure 5.4.

5.4.3 Fabrication of the electrochemical immunosensor

For the β-lactoglobulin measurements, required concentrations of antibodies β-LG were prepared in 10 mM PBS buffer pH 7.4, solution was pipetted onto the vials, which has magnetic FeC@Graphene nanoparticles and was incubated for 45 minutes. After the immobilization of β-LG antibodies upon the surface of magnetic FeC@Graphene nanoparticles antibodies can be held onto vials. Obtained immunosensor was immersed into β-LG solution to complete an antigen-antibody

interaction for 45 minutes. Then, the modified nanoparticles were washed with PBS solution and were extracted from vials by using a magnet filed to cover the working area of the screen-printed carbon electrodes (SPCEs) and dried in vacuo.

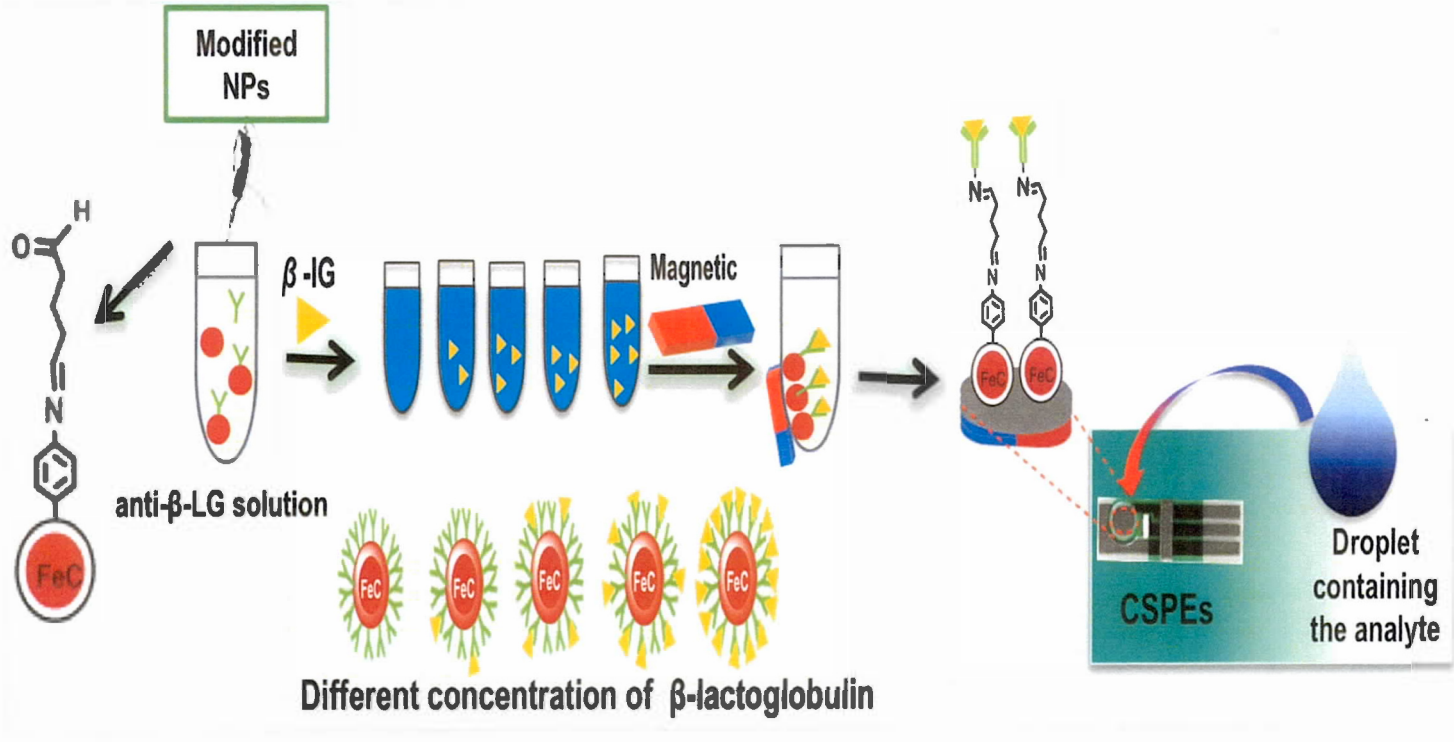

Figure 5. 4 Schematic illustration of the stepwise immunosensor fabrication process (M.Alahmadi, 2016)

5.4.4 Electrochemical measurements of immunosensors

For the detection of β-lactoglobulin, the immunosensors were incubated with different concentrations of β-lactoglobulin solution (0, 0.0001, 0.001, 0.01, 0.1, 1, 10 and 100 $ngmL^{-1}$) for 45 minutes. Therefore, electrochemical immunosensor based on using modified FeC@Graphene NPs was successfully obtained and stored at 4 °C for the following experiment. Then the (CSPEs) electrode was washed with PBS, and then extracts NPs from the first low concentration solution of β-lactoglobulin and dropped it onto the carbon-working electrode surface and incubated for 30 min at room temperature. Finally, when the first measurement has been done, the electrode was cleaned carefully with PBS in order to use respectively modified NPs with different concentrations of β-lactoglobulin. All the electrochemical measurements were performed in 10 mM PBS (pH 7.0) containing 5.0 mM $[Fe(CN)_6]^{-3/-4}$ redox pair square wave voltammetry (SWV) at room temperature. Square wave voltammetry were obtained between the range of 0.4 V and -0.4 V at a scan rate of 100 mVs^{-1}.

5.4.5 Detection of β-lactoglobulin

Square wave voltammetry (SWV) have been employed to characterize the fabrication process of the immunosensor by using $[Fe(CN)_6]^{-3/-4}$ redox probe. SWV was used to indicate the fabrication process of the electrochemical immunosensor by obtaining the peak current. Figure 5.5 demonstrates the squarewave voltammetry (SWV)

voltammograms for the Immunosensor gained from immunochemical reaction of various concentrations of β-lactoglobulin (0, 0.0001, 0.001, 0.01, 0.1, 1, 10 and 100ng/mL) with the antibody. As depicted from Fig.5.4 Show that the decrease in current response was proportional to the β-lactoglobulin concentration in the range of 1 to 100 ng/mL. The maximum peak current value at SWV voltammograms was obtained with the immobilization of zero ng/mL concentration of β-LG on the modified NPs with antibodies. With increasing concentration of β-lactoglobulin, there were gradually decrease in the squarewave voltammetry SWV reduction peak of $[Fe(CN)_6]^{4-/3-}$. For this reason, a significant decrease at SWV peak current was obtained due to an immune reaction of antibody–antigen complex on the modified electrode surface.

5.4.6 Immunosensor calibration curve

Under optimal experimental conditions, the calibration curve for the immunosensor was plotted for detecting b-lg Fig.5.4. Data from (SWV) voltammograms was used to structure the calibration curve (Figure 5.5 inset). It exhibits a good linear relationship between the changing of the peak currents obtained by SWV and the logarithm of β-lactoglobulin concentrations from the range of 0.1 $pgml^{-1}$ to 100 $ngml^{-1}$. The linear regression equation of y = -8E-08x + 3E-07, and correlation coefficient of 0.9909.The detection limit (LOD) value was estimated to be 0.01 pg/mL. This sensor proved to be very sensitive and for low level of β-lg detection in buffer solutions.

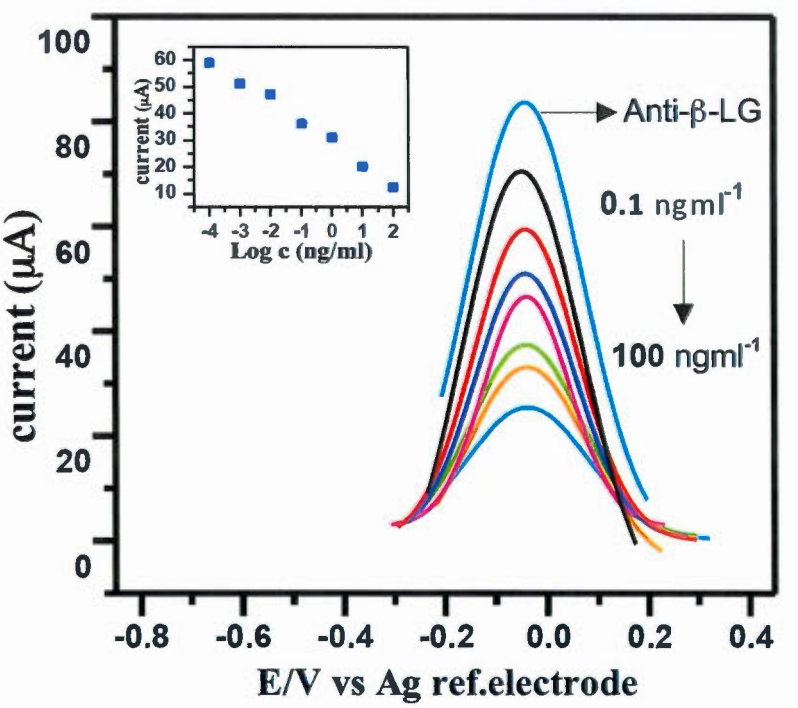

Figure 5. 5 (SWV) of the immunosensor incubated with different concentrations of β-lactoglobulin (0.1 to 100 $ngml^{-1}$): the concentrations of β-LG are 0.000, 0.0001. 0.001, 0.01, 0.1, 1.0, 10 and 100 $ngml^{-1}$. The inset is the calibration curve shows the relationships between the changing of SWV peak currents of the immunosensor and the increasing of the logarithm concentration of β-LG.

5.5. Conclusions

In summary, the developed a novel electrochemical immunosensor based on deposition modified FeC@Graphene NPs on working electrode using carbon screen-printed electrode for the detection of β-lactoglobulin was developed. The FeC@Graphene NPs was first modified with P-nitro phenyl, P-aminophenyl, and β-lactoglobulin antibodies, which was subsequently immobilized on the surface FeC@Graphene NPs with glutaraldehyde cross-linker for direct detection of β-lactoglobulin via an antigen-antibody immunochemical reaction. Furthermore, by using external magnetic field, this is method to separate biomolecules that does not bind with modified NPs or free PBS buffer. The fabrication immunosensor was monitored by using squarewave voltammetry SWV when the surface functionalization by binding β-lactoglobulin. The performance of this sensor was evaluated in terms of its sensitivity, detection limit, and dynamic range. The present immunosensor successfully detected β-lg down to 0.01pg/mL in linear range 0.1-100 ng/mL.

CHAPTER VI

CONCLUSIONS

In this study, a unique one-step growth method of ferromagnetic and superparamagnetic nanoparticles is presented. The high-density and well-dispersed core-shell FeC@Graphene nanoparticles (NPs) were obtained on the top of graphene multilayers covering copper foils in a single-stage furnace after chemical vapor deposition which was performed using ferrocene at high temperatures, up to 950℃.
The magnetic properties have been proven by utilization hysteresis curve. The Raman spectrum has shown the existence of iron and carbon, and the particle size increase by increasing the temperature whereas the SEM and TEM images confirmed that the synthesized nanoparticles have nano-size roughly 50 to 80 nm, and the core-shell structure of NPs is well resolved where a spherical FeC core is surrounded by about 5 to 10 nm graphene layers. The resulting magnetic FeC@Graphene NPs were used to fabricate a sensitive immunosensor for β-lactoglobulin detection by using layer functionalizations. It was demonstrated the covalent functionalization for FeC @Graphene NPs, in first place, grafting nitro groups were introduced to the surface of iron nanoparticles by spontaneous reaction with 4-nitrobenzenediazonium tetrafluoroborate (*P*-NBDT) to form 4-nitrobenzene. In the second place the covalent grafting of aminophenyl functionalized magnetic nanoparticles through the reduction of 4-nitro phenyl on surface FeC@Graphene has been confirmed by using FT-IR spectroscopy. The absence of the characteristic peaks of nitro group (1378 cm^{-1} and

1565 cm^{-1}) and the presence of new peaks corresponding to amino groups (3300 cm^{-1}) confirmed the reduction of nitro groups. Glutaraldehyde was used as cross-linker to immobilize antibodies effectively through the formation of imine bonds. Finally, Anti-β-lactoglubulin, which has amine terminal groups, was successfully immobilized on these activated magnetic nanoparticles. The resulting functionalized graphene-coated iron carbide NPs allows a significant immobilization of β-lactoglubulin, and improving the sensitivity of the immunosensor. The development of a novel electrochemical immunosensor based on modified FeC@Graphene NPs deposited on carbon as working electrode by using carbon screen-printed electrode for the detection of β-lactoglobulin was achieved. The anti-β-lactoglobulin functionalized FeC@Graphene NPs were used for detection of β-lactoglobulin via an antigen antibody immunochemical reaction. Furthermore, by using external magnetic field is an easy and novel method to detach biomolecules that does not bind with modified FeC@Graphene NPs or free PBS buffer. The fabricated immunosensor was monitored by using squarewave voltammetry (SWV) to follow the change in the electron transfer after binding β-lactoglobulin by the functionalized electrode surface. The performance of this sensor was evaluated in terms of its sensitivity, detection limit, and dynamic range. The present immunosensor successfully detected β-lg down to 0.01 pg/mL in linear range of 0.1-100 ng/mL.

BIBLIOGRAPHY

{In-Yup Jeon, Dong Wook Chang, Nanjundan Ashok Kumar, J.-B. B. (2011). Functionalization Of carbon nanotubes. In *Carbon Nanotubes - Polymer Nanocomposites* (pp. 1–203). Cleveland, Ohio, 1South Korea ,2USA. Retrieved from http://www.intechopen.com/books/export/citation/BibTex/carbon-nanotubes-polymer-nanocomposites/functionalization-of-carbon-nanotubes}

Actis, P., Caulliez, G., Shul, G., Opallo, M., Mermoux, M., Marcus, B., … Szunerits, S. (2008). Functionalization of glassy carbon with diazonium salts in ionic liquids. *Langmuir*, *24*(29), 6327–6333. doi:10.1021/la703714a

Akbarzadeh, A., Samiei, M., & Davaran, S. (2012). Magnetic nanoparticles: preparation, physical properties, and applications in biomedicine. *Nanoscale Research Letters*, *7*, 144. doi:10.1186/1556-276X-7-144

Amara, D., Grinblat, J., & Margel, S. (2012). Solventless thermal decomposition of ferrocene as a new approach for one-step synthesis of magnetite nanocubes and nanospheres. *Journal of Materials Chemistry*, *22*, 2188. doi:10.1039/c1jm13942h

Amendola, V., & Meneghetti, M. (2009). Laser ablation synthesis in solution and size manipulation of noble metal nanoparticles. *Physical Chemistry Chemical Physics : PCCP*, *11*, 3805–3821. doi:10.1039/b900654k

Andersen, K. E., Fong, C. Y., & Pickett, W. E. (2002). Quantum confinement in CdSe nanocrystallites. *Elsevier Science*, *302*, 1105–1110.

Andrade, a L., Souza, D. M., Pereira, M. C., Fabris, J. D., Domingues, R. Z., Federal, U., … Horizonte, B. (2009). Synthesis and characterization of magnetic nanoparticles coated with silica through a sol-gel approach (Síntese e

caracterização de nanopartículas magnéticas revestidas com sílica através de um processo sol-gel). *Nano*, *55*, 420–424.

Aoki, T., Iskandar, S., Yoshida, T., Takahashi, K., & Hattori, M. (2006). Reduced immunogenicity of beta-lactoglobulin by conjugating with chitosan. *Bioscience, Biotechnology, and Biochemistry*, *70*(10), 2349–2356. doi:10.1271/bbb.50398

Aviv, G. (2008). Superconducting Quantum Interference Devices 1. *SQUIDs-Superconducting Quantum Interference Devices*, 1–9.

Bekyarova, E., Itkis, M. E., Ramesh, P., Berger, C., Sprinkle, M., De Heer, W. a., & Haddon, R. C. (2009). Chemical modification of epitaxial graphene: Spontaneous grafting of aryl groups. *Journal of the American Chemical Society*, *131*(2), 1336–1337. doi:10.1021/ja8057327

Bhowmick, S. (2012). X-Ray Diffraction and its Prospects in Power Generation, *5*(1), 1–12.

Black, R. C., & Wellstood, F. C. (2006). *Measurements of Magnetism and Magnetic Properties of Matter. Applications of SQUIDs and SQUID Systems* (Vol. 2, pp. 391–440). doi:10.1002/9783527609956.ch12

Chaitoglou, S., Sanaee, M. R., & Bertran, E. (2014). Arc-Discharge Synthesis of Iron Encapsulated in Carbon Nanoparticles for Biomedical Applications, *2014*, 8. Retrieved from http://dx.doi.org/10.1155/2014/178524

Choy, K. (2003). Chemical vapour deposition of coatings. *Progress in Materials Science*, *48*, 57–170. doi:10.1016/S0079-6425(01)00009-3

Chukwuocha, E. O. (2012). Theoretical Studies on the Effect of Confinement on Quantum Dots Using the Brus Equation. *World Journal of Condensed Matter Physics*, *02*(May), 96–100. doi:10.4236/wjcmp.2012.22017

Cnms, N., Bhattacharjee, C. R., & Nath, A. (2012). Chemical Vapour Deposition (CVD) Technique and the Synthesis of Carbon, *4*(1), 706–713.

Crespi, V. H. (2004). The Geometry of Nanoscale Carbon. *Introduction to Nanoscale Science and Technology*, (Figure 1), 103–118. doi:10.1007/1-4020-7757-2_5

Croguennec, T., Mollé, D., & Mehra, R. A. J. (2004). Spectroscopic characterization of heat-induced nonnative NL -lactoglobulin monomers, 1340–1346. doi:10.1110/ps.03513204.1340

Davydov, V., Rakhmanina, A., Kireev, I., Alieva, I., Zhironkina, O., Strelkova, O., ... Khabashesku, V. (2014). Solid state synthesis of carbon-encapsulated iron carbide nanoparticles and their interaction with living cells. *Journal of Materials Chemistry B*. doi:10.1039/c3tb21599g

De La Escosura-Muñiz, A., Parolo, C., & Merkoi, A. (2010). Immunosensing using nanoparticles. *Materials Today*, *13*(7), 24–34. doi:10.1016/S1369-7021(10)70125-5

Dolgaev, S. I., Simakin, a. V., Voronov, V. V., Shafeev, G. a., & Bozon-Verduraz, F. (2002). Nanoparticles produced by laser ablation of solids in liquid environment. *Applied Surface Science*, *186*, 546–551. doi:10.1016/S0169-4332(01)00634-1

Domènech, B., Bastos-Arrieta, J., Alonso, A., Macanás, J., Muñoz, M., & Muraviev, D. N. (2012). Bifunctional Polymer-Metal Nanocomposite Ion Exchange Materials. *Ion Exchange Technologies*, 35–72. doi:http://dx.doi.org/10.5772/51579

Edwards, H. G. M. (2005). *Modern Raman Spectroscopy—A Practical Approach. Journal of Raman Spectroscopy* (Vol. 36, pp. 835–835). doi:10.1002/jrs.1320

Eissa, S., Tlili, C., L'Hocine, L., & Zourob, M. (2012). Electrochemical immunosensor for the milk allergen ??-lactoglobulin based on electrografting of organic film on graphene modified screen-printed carbon electrodes. *Biosensors and Bioelectronics*, *38*(1), 308–313. doi:10.1016/j.bios.2012.06.008

Fan, N., Ma, X., Ju, Z., & Li, J. (2008). Formation, characterization and magnetic properties of carbon-encapsulated iron carbide nanoparticles. *Materials Research Bulletin*, *43*, 1549–1554. doi:10.1016/j.materresbull.2007.06.017

Fedoseeva, Y. V., Bulusheva, L. G., Okotrub, a. V., Vyalikh, D. V., Huo, J., Song, H., ... Chen, X. (2012). Effect of oxidation and heat treatment on the morphology and electronic structure of carbon-encapsulated iron carbide nanoparticles. *Materials Chemistry and Physics*, *135*(1), 235–240. doi:10.1016/j.matchemphys.2012.04.063

Ferrari, A. C. (2007). Raman spectroscopy of graphene and graphite: Disorder, electron-phonon coupling, doping and nonadiabatic effects. *Solid State Communications*, *143*, 47–57. doi:10.1016/j.ssc.2007.03.052

Fultz, B., & Howe, J. M. (2007). *Transmission Electron Microscopy and Diffractometry of Materials* (pp. 1–57). doi:10.1007/978-3-642-29761-8

Ghosh, S. K. (2011). Kubo Gap as a Factor Governing the Emergence of New Physicochemical Characteristics of the Small Metallic Particulates. *Science and Technology*, 114–121.

Greenberg, Y. S. (1998). Application of superconducting quantum interference devices to nuclear magnetic resonance. *Reviews of Modern Physics*, *70*(1), 175–222. doi:10.1103/RevModPhys.70.175

Guozhong Cao, Y. W. (2010). *Nanostructures and Nanomaterials: Synthesis, Properties, and Applications* (Vol. 3, pp. 61–71). London. Retrieved from https://books.google.ca/books?isbn=9814324558

Häfeli, U. O. (2004). Magnetically modulated therapeutic systems. *International Journal of Pharmaceutics*, *277*(August 2002), 19–24. doi:10.1016/j.ijpharm.2003.03.002

Hodkiewicz, J. (210AD). Characterizing Carbon Materials with Raman Spectroscopy. *Application Note: 51901*, 1–5.

Hodkiewicz, J. (2010). Characterizing Graphene with Raman Spectroscopy, Application note: 51946.

Horikoshi, S. and Serpone, N. (2013). Introduction to Nanoparticles. In *Microwaves in Nanoparticle Synthesis: Fundamentals and Applications* (pp. 1–24). Weinheim, Germany. doi:10.1002/9783527648122.ch1

Hossain, M. Z., Walsh, M. a., & Hersam, M. C. (2010). Scanning Tunneling Microscopy, Spectroscopy, and Nanolithography of Epitaxial Graphene Chemically Modified with Aryl Moities. *Journal of the American Chemical Society*, *132*(29), 15399–15403.

Huber, D. L. (2005). Synthesis, properties, and applications of iron nanoparticles. *Small*, *1*(5), 482–501. doi:10.1002/smll.200500006

Huo, J., Song, H., & Chen, X. (2004). Preparation of carbon-encapsulated iron nanoparticles by co-carbonization of aromatic heavy oil and ferrocene. *Carbon*, *42*, 3177–3182. doi:10.1016/j.carbon.2004.08.007

Ibrahim, A. S. S., Al-Salamah, A. a., El-Toni, A. M., El-Tayeb, M. a., & Elbadawi, Y. B. (2013). Immobilization of cyclodextrin glucanotransferase on aminopropyl-functionalized silica-coated superparamagnetic nanoparticles. *Electronic Journal of Biotechnology*, *16*. doi:10.2225/vol16-issue6-fulltext-8

Ikeguchi, M. (2014). Transient Non-Native Helix Formation during the Folding of b-Lactoglobulin. *Biomolecules*, *4*(Figure 1), 202–216. doi:10.3390/biom4010202

Inagaki, M. (2012). Carbon coating for enhancing the functionalities of materials. *Carbon*, *50*(9), 3247–3266. doi:10.1016/j.carbon.2011.11.045

Jahanshahi, M., & Kiadehi, A. (2013). Fabrication, Purification and Characterization of Carbon Nanotubes: Arc-Discharge in Liquid Media (ADLM). *Syntheses and Applications of Carbon Nanotubes and Their Composites*, 55–76. doi:10.5772/51116

John F. Mongillo. (2007). Nanotechnology 101. In *Nanotechnology 101* (p. 63). Westport, Conn. : Greenwood Press, 2007.

Katsnelson, M. I. (2007). Graphene: carbon in two dimensions. *Materials Today*, *10*(1), 20–27. doi:10.1016/S1369-7021(06)71788-6

Knipping, P., & Laue, M. Von. (1952). X-ray Diffraction, 1–18.

Kolhatkar, A. G., Jamison, A. C., Litvinov, D., Willson, R. C., & Lee, T. R. (2013). *Tuning the magnetic properties of nanoparticles. International Journal of Molecular Sciences* (Vol. 14, pp. 15977–16009). doi:10.3390/ijms140815977

Komogortsev, S. V., Iskhakov, R. S., Balaev, a. D., Kudashov, a. G., Okotrub, a. V., & Smirnov, S. I. (2007). Magnetic properties of Fe3C ferromagnetic nanoparticles encapsulated in carbon nanotubes. *Physics of the Solid State*, *49*(4), 734–738. doi:10.1134/S1063783407040233

Kosynkin, D., Bockman, T. M., & Kochi, J. K. (1997). Thermal (iodide) and photoinduced electron-transfer catalysis in biaryl synthesis via aromatic arylations with diazonium salts. *Journal of the American Chemical Society*, *119*(4), 4846–4855. doi:10.1021/ja970599b

Kumar, A., & Lee, C. H. (2013). Synthesis and Biomedical Applications of Graphene : Present and Future Trends. *Advances in Graphene Science*, 55–75. doi:10.5772/55728

Lancelot, E., Lille, D., & Ascq, V. (n.d.). Perspectives on Raman Spectroscopy of Graphene. *Horiba Scientific*.

Lian, W., Song, H., Chen, X., Li, L., Huo, J., Zhao, M., & Wang, G. (2008). The transformation of acetylene black into onion-like hollow carbon nanoparticles at

1000 ??C using an iron catalyst. *Carbon*, *46*, 525–530. doi:10.1016/j.carbon.2007.12.024

Lim, H., Lee, J. S., Shin, H. J., Shin, H. S., & Choi, H. C. (2010). Spatially resolved spontaneous reactivity of diazonium salt on edge and basal plane of graphene without surfactant and its doping effect. *Langmuir*, *26*(14), 12278–12284. doi:10.1021/la101254k

Luo, N., Li, X., Wang, X., Yan, H., Zhang, C., & Wang, H. (2010). Synthesis and characterization of carbon-encapsulated iron/iron carbide nanoparticles by a detonation method. *Carbon*, *48*(13), 3858–3863. doi:10.1016/j.carbon.2010.06.051

M.Alahmadi. (2016). *MAGNETIC CARBON-ENCAPSULATED IRON CARBIDE NANOPARTICLES: SYNTHESIS, FUNCTIONALIZATION, AND APPLICATION*. Université du Québec à Montréal.

Madhavi, V., Prasad, T., & Madhavi, G. (2013). Synthesis and Spectral Characterization of Iron Based Micro and Nanoparticles. *International Journal of Nanomaterials and Biostructures*, *3*(2), 31–34. doi:10.5829/idosi.ijee.2013.04.04.10

Matsue, T., Yamada, Y., & Kobayashi, Y. (2012). Iron carbide nanoparticles produced by laser ablation in organic solvent. *Hyperfine Interactions*, *205*, 31–35. doi:10.1007/s10751-011-0452-z

Mody, V. V., Singh, A., & Wesley, B. (2013). Basics of magnetic nanoparticles for their application in the field of magnetic fluid hyperthermia. *European Journal of Nanomedicine*, *5*(1), 11–21. doi:10.1515/ejnm-2012-0008

Moina, C., & Ybarra, G. (2012). Fundamentals and Applications of Immunosensors. *Advances in Immunoassay Technology*, 65–80. doi:10.5772/36947

Mura, S., Greppi, G., Marongiu, M. L., Roggero, P. P., Ravindranath, S. P., Mauer, L. J., … Irudayaraj, J. (2012). FTIR nanobiosensors for Escherichia coli detection. *Beilstein Journal of Nanotechnology*, *3*, 485–492. doi:10.3762/bjnano.3.55

Murphy, D. M., Cullen, R. J., Jayasundara, D. R., Scanlan, E. M., & Colavita, P. E. (2012). Study of the spontaneous attachment of polycyclic aryldiazonium salts onto amorphous carbon substrates. *RSC Advances*, *2*, 6527. doi:10.1039/c2ra20292a

Mwamba, I. A. (2005). Characterisation of Al-Ti-B grain refiners prepared by aluminothermic reduction of TiO2 and B2O3. *Review Literature And Arts Of The Americas*, (2006-11-14T11:26:37Z), 15–42. Retrieved from http://hdl.handle.net/10539/1687

Oropeza, S., Corea, M., Gómez-Yáñez, C., Cruz-Rivera, J. J., & Navarro-Clemente, M. E. (2012). Zero-valent iron nanoparticles preparation. *Materials Research Bulletin*, *47*, 1478–1485. doi:10.1016/j.materresbull.2012.02.026

Overney, R. (2010). *Nanothermodynamics and Nanoparticle Synthesis , Nanoparticles, Part, 24-27,Course nanoscience and Molecular Engineering(ChemE498A)*. University of Washington. Retrieved from http://courses.washington.edu/overney/NME498_Material/NME498_Lectures/Lecture on Thermo and Nanoparticles v5.pdf

Pankhurst, Q. a, Connolly, J., Jones, S. K., & Dobson, J. (2003). Applications of magnetic nanoparticles in biomedicine. *Journal of Physics D: ...*, *167*, R167–R181. doi:10.1088/0022-3727/36/13/201

Patel, R. K., Chauhan, J. B., Singh, K. M., & Soni, K. J. (2007). Allelic frequency of kappa-casein and beta-lactoglobulin in Indian crossbred (Bos taurus x Bos indicus) dairy bulls. *Turkish Journal of Veterinary and Animal Sciences*, *31*(6), 399–402.

Peng, L. M., Dudarev, S., & Whelan, M. (2005). *High Energy Electron Diffraction and Microscopy* (pp. 8–9). Oxford University Press. Retrieved from https://books.google.ca/books?id=nUZTYtrDEIkC&printsec=frontcover&source=gbs_ge_summary_r&cad=0#v=onepage&q&f=false

Petkova, G. a, Záruba, K., Žvátora, P., & Král, V. (2012). Gold and silver nanoparticles for biomolecule immobilization and enzymatic catalysis. *Nanoscale Research Letters*, *7*, 287. doi:10.1186/1556-276X-7-287

Quintana, M., Spyrou, K., & Grzelczak, M. (2010). Functionalization of graphene via 1, 3-dipolar cycloaddition. *Acs ...*, *4*(6), 3527–3533. Retrieved from http://pubs.acs.org/doi/abs/10.1021/nn100883p

Rai, R. S., & Subramanian, S. (2009). Role of transmission electron microscopy in the semiconductor industry for process development and failure analysis. *Progress in Crystal Growth and Characterization of Materials*, *55*(3-4), 63–97. doi:10.1016/j.pcrysgrow.2009.09.002

Ramanathan, T., Fisher, F. T., Ruoff, R. S., & Brinson, L. C. (2005). Amino-fimctionalized carbon nanotubes for binding to polymers and biological systems. *Chemistry of Materials*, *17*(8), 1290–1295. doi:10.1021/cm048357f

Ramírez, N. B., Salgado, a. M., & Valdman, B. (2009). The evolution and developments of immunosensors for health and environmental monitoring: Problems and perspectives. *Brazilian Journal of Chemical Engineering*, *26*(02), 227–249. doi:10.1590/S0104-66322009000200001

Reithmeier, E., Vynnyk, T., & Schultheis, T. (2010). 3D-measurement using a scanning electron microscope. *Applied Mathematics and Computation*, *217*(3), 1193–1201. doi:10.1016/j.amc.2010.01.107

Rik Brydson1, Andy Brown1, L. G. B. (2005). Analytical Transmission Electron Microscopy. *Materials Research*, *35*, 239–314. doi:10.1146/annurev.matsci.35.102303.091623

Rocha, J. M. S., Gil, M. H., & Garcia, F. a P. (1998). Effects of additives on the activity of a covalently immobilised lipase in organic media. *Journal of Biotechnology*, *66*, 61–67. doi:10.1016/S0168-1656(98)00157-6

Roduner, E. (n.d.). Physics and Chemistry of Nanostructures: Why nano is different. *Encyclopedia of Life Support Systems (EOLSS)*.

Roduner, E. (2006). Size matters: why nanomaterials are different. *Chemical Society Reviews*, *35*(March), 583–592. doi:10.1039/b502142c

Ronkainen, N. J., & Okon, S. L. (2014). Nanomaterial-based electrochemical immunosensors for clinically significant biomarkers. *Materials*, *7*, 4669–4709. doi:10.3390/ma7064669

Scott, R. a. (2007). *Applications of physical methods to inorganic and bioinorganic chemistry* (p. 146). Wiley. Retrieved from http://books.google.com/books?id=BA7P4TGdqv4C&pgis=1

Si, P., Zhang, Z., Geng, D., You, C., Zhao, X., & Zhang, W. (2003). 11. Synthesis and characteristics of carbon-coated iron and nickel nanocapsules produced by arc discharge in ethanol vapor.pdf. *Elsevier Science*, *41*, 247–251.

Singh, S. C., & Gopal, R. (2007). Zinc nanoparticles in solution by laser ablation technique. *Bulletin of Materials Science*, *30*(3), 291–293. doi:10.1007/s12034-007-0048-z

Singh, V., Joung, D., Zhai, L., Das, S., Khondaker, S. I., & Seal, S. (2011). Graphene based materials: Past, present and future. *Progress in Materials Science*, *56*(8), 1178–1271. doi:10.1016/j.pmatsci.2011.03.003

Skládal, P., Kovář, D., Krajíček, V., Krajíček, P., Přibyl, J., & Švábenská, E. (2013). Electrochemical immunosensors for detection of microorganisms. *International Journal of Electrochemical Science*, *8*, 1635–1649.

Smith, E., Dent, G., & Wiley, N. J. (2013). Basic Theory. In *Modern raman spectroscopy : a practical approach* (p. 4). Hoboken, N.J. : Wiley, 2013.

Spies, J. 1973 . J. Milk Food Technol., 36: 225–231. (n.d.).

Stefanaki, E. (2008). Electron Microscopy, 1–11.

Suga, M., Asahina, S., Sakuda, Y., Kazumori, H., Nishiyama, H., Nokuo, T., … Terasaki, O. (2014). Recent progress in scanning electron microscopy for the characterization of fine structural details of nano materials. *Progress in Solid State Chemistry*, *42*(1-2), 1–21. doi:10.1016/j.progsolidstchem.2014.02.001

Sun, Y.-P., Li, X., Cao, J., Zhang, W., & Wang, H. P. (2006). Characterization of zero-valent iron nanoparticles. *Advances in Colloid and Interface Science*, *120*, 47–56. doi:10.1016/j.cis.2006.03.001

Thanh, N. T. K., Maclean, N., & Mahiddine, S. (2014). Mechanisms of nucleation and growth of nanoparticles in solution. *Chemical Reviews*, *114*(1), 7610–30. doi:10.1021/cr400544s

Thomas, P. J., & Kulkarni, G. U. (2003). From colloids to nanotechnology: Investigations on magic nuclearity palladium nanocrystals. *Current Science*, *85*(12), 1760–1766.

Tiago, M. L., Zhou, Y., Alemany, M. M. G., Saad, Y., & Chelikowsky, J. R. (2006). Evolution of magnetism in iron from the atom to the bulk. *Physical Review Letters*, *97*. doi:10.1103/PhysRevLett.97.147201

To, P. S. (1999). *Providing Solution to your Diffraction Needs Chapter 7 : Basics of X-ray Diffraction. Solutions* (pp. 1–25). Retrieved from http://epswww.unm.edu/xrd/xrdbasics.pdf

Tully, E., Higson, S. P., & O'Kennedy, R. (2008). The development of a "labeless" immunosensor for the detection of Listeria monocytogenes cell surface protein,

Internalin B. *Biosensors and Bioelectronics*, *23*, 906–912. doi:10.1016/j.bios.2007.09.011

Uliana, C. V. (2014). Diagnostic tests for hepatitis C: Recent trends in electrochemical immunosensor and genosensor analysis. *World Journal of Gastroenterology*, *20*(42), 15476. doi:10.3748/wjg.v20.i42.15476

Vatta, L. L., Sanderson, R. D., & Koch, K. R. (2006). Magnetic nanoparticles : Properties and potential applications. *Advanced Materials*, *78*(9), 1793–1801. doi:10.1351/pac200678091801

Wagener, P., Barcikowski, S., Bärsch, N., & Gmbh, P. (2011). Fabrication of nanoparticles and nanomaterials using laser ablation in liquids. *Laser Technology*, 2–5.

Wagner, L. C. (Ed. . (1999). *Failure Analysis of Integrated Circuits* (pp. 205–215). doi:10.1007/978-1-4615-4919-2_12

Wang, Z. (2000). Transmission electron microscopy of shape-controlled nanocrystals and their assemblies. *The Journal of Physical Chemistry B*, *104*, 1153–1175. doi:10.1021/jp993593c

Wu, W., He, Q., & Jiang, C. (2008). Magnetic iron oxide nanoparticles: Synthesis and surface functionalization strategies. *Nanoscale Research Letters*, *3*, 397–415. doi:10.1007/s11671-008-9174-9

Yang, G. W. (2007). Laser ablation in liquids: Applications in the synthesis of nanocrystals. *Progress in Materials Science*, *52*, 648–698. doi:10.1016/j.pmatsci.2006.10.016

Zhang, H., Liang, C., Liu, J., Tian, Z., & Shao, G. (2013). The formation of onion-like carbon-encapsulated cobalt carbide core/shell nanoparticles by the laser ablation of metallic cobalt in acetone. *Carbon*, *55*(iv), 108–115. doi:10.1016/j.carbon.2012.12.015

Zhou, J., Du, L., Zou, L., Zou, Y., Hu, N., & Wang, P. (2014). An ultrasensitive electrochemical immunosensor for carcinoembryonic antigen detection based on staphylococcal protein A - Au nanoparticle modified gold electrode. *Sensors and Actuators, B: Chemical*, *197*, 220–227. doi:10.1016/j.snb.2014.02.009

Zhu, H., Huang, P., Jing, L., Zuo, T., Zhao, Y., & Gao, X. (2012). Microstructure evolution of diazonium functionalized graphene: A potential approach to change

graphene electronic structure. *Journal of Materials Chemistry*, *22*, 2063. doi:10.1039/c1jm14862a